POLITECNICO DI TORINO

Corso di Laurea in Ingegneria Meccanica

Tesi di Laurea Magistrale

Wave propagation in phononic stubbed metamaterials

Numerical and experimental characterization

Relatore
prof. Stefano Marchesiello

Correlatore:
prof. Alessandro Fasana

Candidato
Matteo Amorusi

University of Minnesota
prof. Stefano Gonella

A.A. 2017-2018

Contents

1 Introduction 1

1.1 Terminology . . . 1
1.2 Relevance . . . 1
1.3 State of the art . . . 3
1.4 Motivation . . . 6
1.5 Statement of work . . . 6

2 Phononic crystal characterization 9

2.1 Geometry . . . 9
2.2 Bloch analysis . . . 11
2.3 Finite Element model . . . 12
2.4 Results from unit cell analysis . . . 15
2.4.1 Dispersion surfaces . . . 15
2.4.2 Band structure . . . 16
2.4.3 Mode shapes . . . 19
2.4.4 Velocities . . . 22
2.5 Summary . . . 26

3 Finite dimensions lattice 29

3.1 Design . . . 29
3.1.1 Phononic characteristics . . . 30
3.1.2 Manufacturing aspects . . . 34
3.1.3 Final design . . . 36
3.1.4 The specimen . . . 37
3.2 Numerical steady state simulation . . . 40
3.2.1 FE model of the specimen . . . 40
3.2.2 Results . . . 41
3.3 Experimental test . . . 48
3.3.1 Setup and measurement . . . 48
3.3.2 Results and comparison . . . 50
3.4 Numerical transient simulation . . . 55

4 Conclusions 59

Bibliography 61

Summary

The present work deals with some classical phenomena observed in the field of wave propagation in periodic structures, namely the ability to act as band filters and to trigger preferential directions of propagation for specific frequencies.

After a brief presentation of the theoretical backgrounds, a numerical and experimental characterization of the phononic features is provided. The former have been carried out by means of a finite element model of both the structure and the elementary unit, the element repeated periodically. This is done because, thanks to the application of periodic boundary conditions derived from the Bloch's theorem, it is possible to analyze the behavior on an infinite lattice taking into account only this unit.

The object of the full scale simulations and experimental test has been designed in order to improve the phononic process sought, facing also issues related to the additive manufacture employed to realize the specimen.

Good agreement has been found between the theoretical prediction and the numerical and experimental characterization, especially in the case of band gap behavior.

Chapter 1

Introduction

1.1 Terminology

A periodic structure is, by definition, a repetition of an elementary unit along one or more directions. The elementary unit itself may belong to either a mono-dimensional or a multi-dimensional domain. Due to the affinity with solid state physics, briefly explained later, it is common to refer to periodic structures as lattices and to elementary units as unit cells. Moreover, structures affecting elastic wave propagation by means of the periodicity of their arrangement are also called *phononic crystals*, in analogy with photonic ones. In a more general fashion, it is possible to refer to these structures as metamaterials, with the meaning of finely tailored assembles achieving unique mechanical properties without any require in terms of periodicity: it just underlines the oddity of these structures. If the waves taken into account are elastic ones, it is common to call such structures acoustic metamaterials. It is worth to notice a certain arbitrariness about these definitions in literature.

There are several possible choices for the elementary unit and different ones can lead to different complexity and calculation times, although results are, as expected, the same. Figure 1.1 shows three different possibilities with increasing complexity for a regular hexagonal lattice. Later it will be clarified how the periodicity directions are affected by this choice.

1.2 Relevance

Periodic structures play a key role thanks to their capability to exhibit peculiar properties: it is indeed possible to obtain such abilities that cannot be found in natural materials and cannot be observed except from a global standpoint, since they concern only the whole structure. It is easy to find examples of periodic structures in nature: honeycombs, for instance, as well as the arrangement of

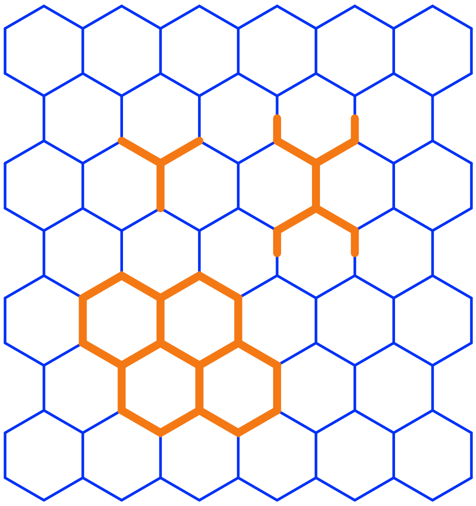

Figure 1.1: Different choices for the unit cell in a regular hexagonal lattice. Actually the two more complex possibilities should have their external boundaries half thick.

atoms in crystals, see Figure 1.2. The above-mentioned implications in solid-state physics would deserve an in-depth analysis that will not be carried out in this work; anyway, this branch of condensed matter physics attempts to relate the periodic characteristics of crystals to their macroscopic properties, mostly conductivities. Moreover, many definitions are borrowed from solid state physics: a phonon is the quantuum mechanical analogous of a vibrational mode since it describes a possible state of excitation of a lattice of interacting particles. The analogy with photons is strong since they both can be interpreted as energy packets with particle-like behavior although solid state physics classifies their nature in two different classes. In the same class of phonons, fermions, are electrons.

Static applications most benefit from the high strength compared to the low global density of these structures: so are mostly made buildings, bridges, and in the aerospace engineering field they are widely used for crucial weight issues. Also weaved textures could be considered periodic arrangements and it is easy to have a sense of the strengthening achieved, as in paper boxes. Although industry still lacks of applications of periodic structures for dynamic purposes, here lies the main appeal for research. Indeed, during the last few decades, a growing amount of works has focused on the acoustic capabilities of phononic crystals. The next section will shortly summarize these studies, focusing on works about acoustic waves propagating in structure with a two dimensional periodicity.

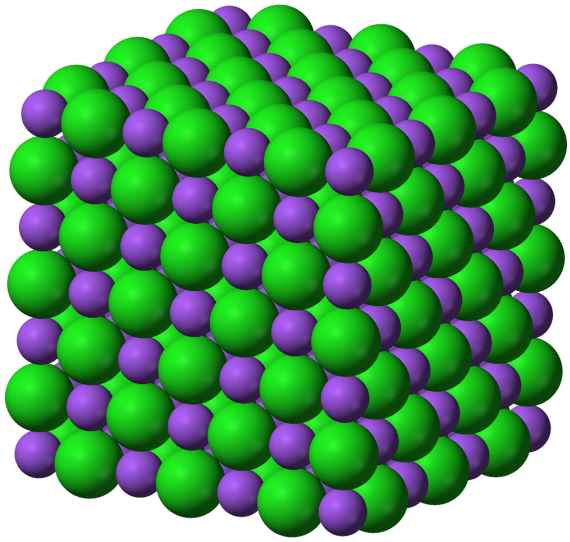

(a) ©Benjah-bmm27

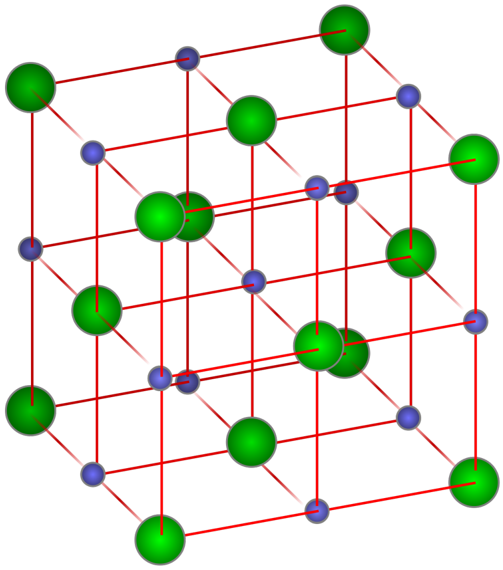

(b) ©Benjah-bmm27

Figure 1.2: (a) Crystal structure of sodium chloride; purple and green spheres represent Na^+ cations and Cl^- anions, respectively. — (b) Unit cell of the lattice.

1.3 State of the art

First studies in the field of periodic structures date back to the works of Newton and Lord Kelvin [12] about mechanical spring-mass chains. During the Twenty-th century Rayleigh [23] and especially Brillouin [2] reintroduced the argument: the latter, indeed, revamped the field working on a variety of problems regarding one-, two- or three-dimensional lattices and being the first to take serious advantage of the Bloch-Floquet's principle. This allows studying the behavior of an infinite periodic structure taking into account a single unit cell and it is definitely the foundation of following works. Later, solid-state physics made a great use of these tools due to the role of electronic structure in defining the properties of crystals, while most of the earlier applications in mechanics put the attention on multi-phase compound materials with inclusions periodically arranged into a matrix.

In the past few decades, several works investigated the features of phononic crystals starting from their band-stop capability. For this topic, very noteworthy is the work of Phani et al. [21] who proposed an interesting comparison between four classes of lattices: triangular, square, hexagonal and Kagomé; they also suggested a strategy for FEM approaches. In a similar way, Gonella and Ruzzene [9] considered the anisotropic behavior of an hexagonal re-entrant lattice which, as a further matter, shows a negative Poisson's ratio. The phenomenon behind this is the Bragg-scattering: the impedance mismatch encountered by a wave propagating in a lattice-like materials leads to destructive inferences; the wavelengths involved in these stop-bands and the spatial periodicity of the structure are comparable.

Liu et al. [15] proposed a first analysis of a locally resonant phononic crystal studying a plate with solid ball coated with silicone rubber and embedded in an epoxy matrix: they obtained low frequencies band gaps ($350 \div 2000$Hz) that would have required huge structures for the activation of the Bragg scattering. This metamaterial was able to stop waves with wavelengths much larger than the characteristic length of resonators, a phenomenon observed with light scattering in gas. They explained how, at resonant frequencies, the energy is trapped by resonator units which thus prevent waves from propagating; moreover, they noticed how these mechanisms require a certain density of resonator cells in the matrix while do not need any periodicity. The same concept has been then investigated on stubbed plates, as the one proposed in this work: Oudich et al. [19] studied the band gap opening in an aluminum thin plate with a two-dimensional arrangement of silicone rubber stubs. Stubbed plate-like phononic crystals have been widely analyzed also for cloaking [5], acoustic rainbow trapping and waveguiding. About the latter two, it is interesting the solution suggested by Celli and Gonella [3] who showed these features by means of a Lego® plate with telescopic resonators. Thanks to these, they have been able to further understand the role of disorder in stubbed plates as they realized a broadband rainbow trap, whose width was enhanced by disorder. They also showed a sub-wavelength waveguide featuring up-shifted resonators instead of an empty path, achieving a better localization of the energy. This happens because the resonators re-transmit the energy to the medium by in-phase waves that interfere constructively with the incoming ones, if the frequency of the excitation is slightly lower than the resonance of the resonators; for this reason the guide become more suitable for energy confinement. Pennec et al. [20] studied periodicity at smaller scale, thus with higher frequency effects, and showed the relation between the geometric and mechanical parameters –such as the height of stubs, their diameter, their distance or the material they are made of– and the band gap position and width. An interesting application is the one proposed by Colombi et al. [6], who succeeded in stopping Rayleigh surface seismic waves employing a tree forest.

Among the above-mentioned unique properties of metamaterials, it is worth to mention the ability to exhibit double-negative effective properties, as theoretically demonstrated by Li and Chan [13]. They considered soft rubber balls dispersed in water obtaining a Poynting vector in opposite direction with the wave vector. This showed up in a simultaneously negative effective bulk modulus and density, which means that the medium expands upon compression and moves to the left when pushed to the right, respectively. This is an acoustic analogue of Veselago's medium [28] in electromagnetism. In addition, when both the effective bulk modulus and the density are negative, the medium can also exhibit negative refraction. A good example for solid media is the work by Zhu et al. [29] in which it is numerically and experimentally demonstrated the possibility to trigger negative refraction at a deep-subwavelength scale by means of a chiral micro-structure. Like in the previous work, this is allowed by a single structure and two different kind of resonances, namely translational and rotational ones, in the ultrasonic range.

Another topic of great interest is the non-linear propagation in periodic structures, started with the first works of Nesterenko [18] about granular chains of identical spheres: a simple model that helps to face the complexity of problem in which is often hard to correlate the abundant amount of parameters to the acoustic properties. Although the source of non-linearity can be manifold, the most investigated one is that coming from the stiffness, and in such granular chains it comes out from the Hertz model of contact, thus with a nearest-neighbor interaction. More recently, Sanchez et al. [24] studied the propagation of nonlinear compressional waves in a one-dimensional granular chain excited at one end by an harmonic force, applying a Fermi-Pasta-Ulam-Tsingou lattice model [7] with quadratic non-linearity (α-FPUT model). Implementing a successive approximation method they analytically showed the generation of second harmonic modes due to a forcing effect of the non-linear interaction. The result is an energy exchange between the two harmonics that is periodic in space. They also illustrated that in the case of evanescent second harmonic, i.e. when the fundamental frequency is greater than half the cutoff, this can not be neglected in the solution at any distance from the forced end. On the same lines, non-linear waveguides featuring internal resonators have been take into account as in the very recent work from Jiao and Gonella [10], which provided a definitive experimental demonstration of intermodal tunneling, i.e. the energy supply to higher frequency modes different in nature from the fundamental one, thanks to second harmonic generation. Indeed, it has been observed the activation of second harmonic axial mechanisms concerning the resonators despite the excitation was out-of-plane at low frequency. Previously they also provided analytical and numerical analysis of the case in [11].

Topology studies are the ones that most borrow from quantuum mechanics investigations: the pursue is to emulate quantuum effects designing a dynamic matrix, and thus a lattice, with characteristics analogue to the Hamiltonian matrix of the Schrödinger's equation. Albeit the classical mechanical formulation of the equations of motion and the description of a quantuum mechanical lattice problem through the Schrödinger's equation differ both for the interpretation of the unknown and for the nature of the problem, the existence of topologically protected edge states is related only to the properties of these matrices and can be detected from an analysis of the band structure. In this way it has been possible to observe reflection-free unidirectional propagation along the edge of the domain with good stability against imperfections [16, 17, 25]. Here the elastic version of the quantuum spin Hall effect (QSHE) is taken into account since two counter-propagating waves are generated along the border and they differ for their spin degree of freedom. Other applications refer to the quantuum valley Hall effect (QVHE) giving birth to topologically protected boundaries modes by means of the space-inverse symmetry breaking along the out-of-plane direction instead of the time reversal symmetry breaking as the former case. This is practically realized designing an edge with respect to which the lattice shows chirality properties [14].

1.4 Motivation

The aim of this study is to account for mechanisms involved in widely investigated phononic processes without a definitive clarification. Indeed, as told in previous sections, phononic properties of locally resonant stubbed plates can be manifold but there is still a lack of connection between the dynamic properties of the resonators and the behavior of the crystal. Since modal analysis of stand alone resonators do not match completely the properties to wave propagation, the goal is to understand what is the resonator, meaning which portion of the unit cell takes part in the storage of energy and how this is constrained by the surrounding crystal.

Furthermore, additive manufacturing capabilities call for an attempt to study wave propagation features as it could allow to test complex structures that could not be realized by standard production. It would not have been possible to manufacture the plate tested in this work without this tool and, on the author's knowledge, no other plates of this kind have been realized without attaching together different parts. However, the process still presents some issues that will be discussed later. Also, the dynamics characteristics of composite material of the kind employed in PolyJet manufacture have been inspected although results obtained are not promising.

1.5 Statement of work

This thesis explores some basic phononic capabilities of an additively manufactured stubbed plate using a three-dimensional FEM model. The study of the lattice properties has been carried out applying Bloch's condition to a single unit cell. Both propagation and stationary case are taken into account and the results obtained have been verified by numerical simulations and experimental test. A Polytec® PSV-400 3D scanning laser Doppler vibrometer has been employed for the experimental characterization, which allows to measure the three components of the velocities without interacting, at least mechanically, with the specimen. The procedure to set up the measure will be illustrated in the specific section. The specimen has been manufactured by the *Earl E. Bakken Medical Device Center* of the University of Minnesota by means of a Stratasys® J750 Polyjet 3D printer. After several attempts, both numerical and experimental, the final design of the unit cell exhibits a mallet-like resonator made of a thin stem connecting the plate to a bulky head. The plate, instead, is made of a square arrangement of seven-by-seven unit cells surrounded by a portion of plain plate. The damping effect of the material employed has been found to be relevant, leading to a relatively small specimen in order to have good imaging quality. Figure 1.3 shows an illustration of the unit cell.

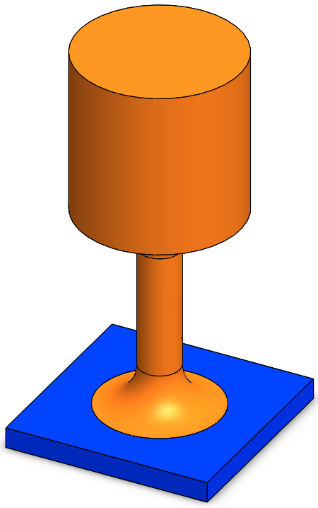

Figure 1.3: Unit cell representation.

The work is organized in four chapters as follows: in the first one a brief introduction to the field of acoustic wave propagation in phononic crystals is given; in the second one the theoretical backgrounds are presented with a special focus to the Bloch's theorem, which is the most powerful tool of the analysis; in the third chapter the numerical and experimental results are summed up and compared. Here the phononic characteristics are illustrated with the selected design as an example, together with a description of the experimental setup and the design process is provided. Eventually, in the last chapter, conclusions to the work and some author's notes are given.

Chapter 2

Phononic crystal characterization

In a general case, to study properties concerning wave propagation in structures one should take into account the information coming from the whole domain. Nevertheless, when a structure is made of a periodic repetition of identical cells, all the information are included into a single unit. This is true when one refer to infinite periodic arrangements, where there is not any information about boundaries to consider. The most straight-forward way to conduct the analysis of such structures looking only at one unit cell is the application of the Bloch's theorem, which employs some clever boundary conditions to input the periodicity information. All the following explanations will be given taking into account the unit cell described above, which features a two-dimensional periodicity in a square arrangement.

A note regarding notation: in the next developments, bold lower case letters indicate vectors, bold capital letters indicate matrices and the italic capital letters reference frames. When the latter appear as superscript of the vectors it states in which reference frame that vector is considered.

2.1 Geometry

In order to create a mathematical model of the lattice, a set of reference frames will be used; the considerations, however, would hold for any choice of reference frame. The first reference frame introduced is a cartesian one with his axes belonging to the lattice plane and defined by the basis $\mathcal{I} = (\hat{\boldsymbol{\imath}}_1, \hat{\boldsymbol{\imath}}_2)$, where the *hat* indicates unit lengths. Here, it is possible to define two *direct lattice* vectors which connect any point in the unit cell with its equivalent in the nearest neighbor cells, as illustrated in Fig. 2.1. Thus, the length of the two vectors is linked to the dimension of the unit cell and to the particular arrangement. Referring to the cartesian reference

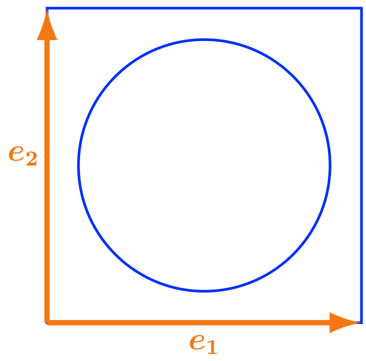

Figure 2.1: Direct lattice vectors on a top view of the unit cell.

frame, the direct lattice vectors of a square lattice are defined

$$\begin{aligned} \boldsymbol{e}_1^{\mathcal{I}} &= (a,0)^{\mathrm{T}} \\ \boldsymbol{e}_2^{\mathcal{I}} &= (0,a)^{\mathrm{T}}. \end{aligned} \tag{2.1}$$

In this way, any cell of the lattice can be identified by means of an integer couple (n_1, n_2) that indicates how many vectors $(\boldsymbol{e}_1, \boldsymbol{e}_2)$ build the path from the reference unit cell. Thus, with respect to the cartesian reference frame, it is possible to write the lattice relation

$$\boldsymbol{\rho}_P(n_1,n_2) = \boldsymbol{r}_P + n_1\boldsymbol{e}_1 + n_2\boldsymbol{e}_2 \tag{2.2}$$

where $\boldsymbol{\rho}_P(n_1,n_2)$ is the position of the generic point belonging to the (n_1,n_2) cell while $\boldsymbol{r}_P$ is the position of the equivalent point in the reference unit cell. The couple (n_1,n_2) is expressed in the direct lattice basis $\mathcal{E} = (\boldsymbol{e}_1, \boldsymbol{e}_2)$ that contains the spatial periodicity of the domain.

At this point, a third reference frame can be considered: the *reciprocal lattice* basis is defined by the vectors $\mathcal{B} = (\boldsymbol{b}_1, \boldsymbol{b}_2)$ that are given by

$$\boldsymbol{b}_i \cdot \boldsymbol{e}_j = \delta_{ij} \tag{2.3}$$

in which δ_{ij} is Kronecker's delta. It follows that $\boldsymbol{b}_1$ will be perpendicular to $\boldsymbol{e}_2$ and $\boldsymbol{b}_2$ to $\boldsymbol{e}_1$. In cartesian coordinates, the reciprocal lattice vectors can be expressed as:

$$\begin{aligned} \boldsymbol{b}_1^{\mathcal{I}} &= \left(\frac{1}{a}, 0\right)^{\mathrm{T}} \\ \boldsymbol{b}_2^{\mathcal{I}} &= \left(0, \frac{1}{a}\right)^{\mathrm{T}}. \end{aligned} \tag{2.4}$$

2.2 Bloch analysis

In order to describe the wave propagation characteristics in a structure describable as seen before, it is usually employed the Bloch's theorem, whose development is shown in the followings starting from the equation of a wave propagating in the lattice. The displacement field $\mathbf{w}(\boldsymbol{r}_P, t)$ in the reference unit cell, as the wave propagates with frequency ω and wave vector $\boldsymbol{k} = \frac{2\pi}{\boldsymbol{\lambda}}$, follows the equation

$$\mathbf{w}(\boldsymbol{r}_P, t) = \mathbf{w}_{P_0} e^{(i\omega t - \boldsymbol{k}\cdot\boldsymbol{r}_P)} \tag{2.5}$$

where $\mathbf{w}_{P_0}$ is the amplitude of the response. The wave vector $\boldsymbol{k}$ can be expressed in the direct lattice space by

$$\boldsymbol{k} = k_1\boldsymbol{e}_1 + k_2\boldsymbol{e}_2 \tag{2.6}$$

in which $k_i = \delta_i + i\epsilon_i$ are complex numbers whose real part δ_i is a measure of the amplitude attenuation from a cell to another and, as in this work, is typically set to 0, while the imaginary part ϵ_i describes the phase change over a unit cell and hence it is called *phase constant*.

Bloch's theorem, seen in this circumstance, states that the displacement at a generic lattice position $\boldsymbol{\rho}_P$, can be evaluated with respect to the equivalent point in the reference unit cell. This can be demonstrated substituting equation (2.2) into (2.5) written for the generic position $\boldsymbol{\rho}_P$

$$\begin{aligned}\mathbf{w}(\boldsymbol{\rho}_P, t) &= \mathbf{w}_{P_0} e^{(i\omega t - \boldsymbol{k}\cdot\boldsymbol{\rho}_P)} = \mathbf{w}_{P_0} e^{[i\omega t - \boldsymbol{k}\cdot(\boldsymbol{r}_P + n_1\boldsymbol{e}_1 + n_2\boldsymbol{e}_2)]} = \\ &= \mathbf{w}(\boldsymbol{r}_P, t) e^{-\boldsymbol{k}\cdot(n_1\boldsymbol{e}_1 + n_2\boldsymbol{e}_2)}\end{aligned} \tag{2.7}$$

According to equation (2.3), one can express the wave vector in the reciprocal lattice space so that equation (2.6) holds:

$$\boldsymbol{k} = \xi_1\boldsymbol{b}_1 + \xi_2\boldsymbol{b}_2. \tag{2.8}$$

Finally, substituting equation (2.8) into (2.7) it can be written:

$$\mathbf{w}(\boldsymbol{\rho}_P, t) = \mathbf{w}(\boldsymbol{r}_P, t) e^{-(n_1\xi_1 + n_2\xi_2)}. \tag{2.9}$$

Here it is clear that the displacement of the generic point $\boldsymbol{\rho}_P$ is described starting from the displacement of the correspondent point in the reference frame multiplied by a term representing a spatial phase shift between cells.

About the direct lattice it has been said that it contains the information about the spatial periodicity of the structure. In the reciprocal lattice, instead, it is described the periodicity of the relation between frequency and wavenumber, namely the *dispersion relation* $\omega = \omega(\boldsymbol{k})$; it is thanks to this periodicity that the infinite lattice can be fully characterized taking into account only one unit cell. The domain that, in the reciprocal basis, contains a single period of this relation and it is centered in the origin is called *first Brillouin zone* and, since it is common that the Brillouin zone shows a certain degree of axial symmetry, it is possible to refer to the *irreducible* Brillouin zone, obtained reducing all the symmetries. The topic will be resumed along with results in order to provide a graphical explanation through them.

2.3 Finite Element model

So far it has been demonstrated that the unit cell and its reciprocal counterpart, the Brillouin zone, contain all the information needed to characterize the lattice. This section will show how this characterization is done employing the Finite Element Method. Specifically, in this work has been exploited a three-dimensional discretization by means of eight-nodes isoparametric hexahedron element with three degree of freedom for each node. In order to obtain such mesh it has been used the free software Gmsh [8] which produced the result in Figure 2.2.

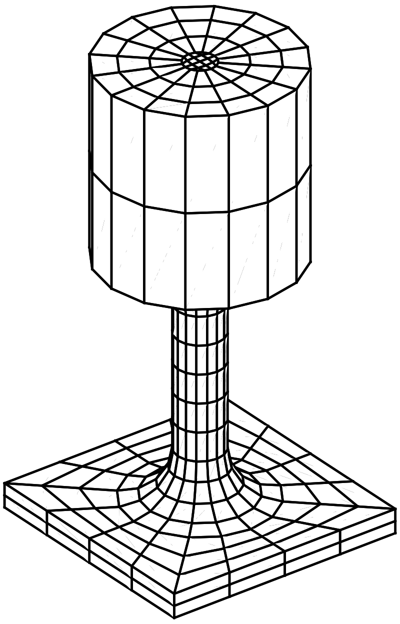

Figure 2.2: Unit cell structured mesh with eight-nodes hexaedron elements.

Once mass matrix $[\mathbf{M}]_{n\times n}$ and stiffness matrix $[\mathbf{K}]_{n\times n}$ have been built, the next step is to apply Bloch's boundary conditions and thus define the periodicity. Indeed, Bloch's conditions relate some boundaries nodes with their opposite along periodicity directions. In the end, this is a reduction allowed by the information of equation (2.9). In the present case, 2D Bloch's conditions have been applied following the scheme illustrated in Figure 2.3 at each layer of nodes the plate is made of.

Labels in Figure 2.3 denote the position of nodes around the boundary: in order to simplify the implementation of Bloch's relations it is now worth to rearrange the generalized coordinates $\{\boldsymbol{u}\}_{n\times 1}$, and thus the rows of the mass and stiffness matrices, grouping degrees of freedom by their position as

$$\{\boldsymbol{u}\} = \{\boldsymbol{u}_L, \boldsymbol{u}_{LB}, \boldsymbol{u}_B, \boldsymbol{u}_I, \boldsymbol{u}_R, \boldsymbol{u}_{LT}, \boldsymbol{u}_{RT}, \boldsymbol{u}_{RB}, \boldsymbol{u}_T\}^{\mathrm{T}} \tag{2.10}$$

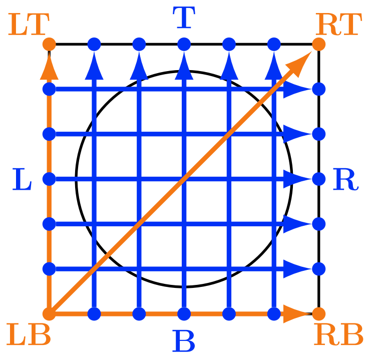

Figure 2.3: Scheme of the application of Bloch's boundary conditions. With a three-dimensional FEM structured mesh this scheme is repeated at each layer of nodes belonging to the plate thickness. Blue labels are meant for the whole edges without corners.

in which $\boldsymbol{u}_I$ refers to all the internal nodes. Now, remembering (2.2), vectors in Figure 2.3 could be described setting values of either one or zero for the couple (n_1, n_2), and in the same way equation (2.9) becomes, as an example, $\boldsymbol{u}_T = \boldsymbol{u}_B e^{i\xi_2}$. According to this, one can assume a reduced vector of generalized coordinates $\{\boldsymbol{u}_r\}_{m\times 1}$ containing only the first four groups of (2.10): internal one and those from which vectors in Figure 2.2 start. The way groups are sorted in (2.10) becomes clear writing the matrix correlating $\{\boldsymbol{u}\}$ and $\{\boldsymbol{u}_r\}$ as follows:

$$\{\boldsymbol{u}\} = \boldsymbol{W}(\xi_1, \xi_2)\{\boldsymbol{u}_r\} \tag{2.11}$$

$$\begin{Bmatrix} \boldsymbol{u}_L \\ \boldsymbol{u}_{LB} \\ \boldsymbol{u}_B \\ \boldsymbol{u}_I \\ \boldsymbol{u}_R \\ \boldsymbol{u}_{LT} \\ \boldsymbol{u}_{RT} \\ \boldsymbol{u}_{RB} \\ \boldsymbol{u}_T \end{Bmatrix} = \begin{bmatrix} [\boldsymbol{I}]_{n_L\times n_L} & [0]_{n_L\times n_{LB}} & [0]_{n_L\times n_B} & [0]_{n_L\times n_I} \\ [0]_{n_{LB}\times n_L} & [\boldsymbol{I}]_{n_{LB}\times n_{LB}} & [0]_{n_{LB}\times n_B} & [0]_{n_{LB}\times n_I} \\ [0]_{n_B\times n_L} & [0]_{n_B\times n_{LB}} & [\boldsymbol{I}]_{n_B\times n_B} & [0]_{n_B\times n_I} \\ [0]_{n_I\times n_L} & [0]_{n_I\times n_{LB}} & [0]_{n_I\times n_B} & [\boldsymbol{I}]_{n_I\times n_I} \\ [\boldsymbol{I}e^{-\xi_1}]_{n_R\times n_L} & [0]_{n_R\times n_{LB}} & [0]_{n_R\times n_B} & [0]_{n_R\times n_I} \\ [0]_{n_{LT}\times n_L} & [\boldsymbol{I}e^{-\xi_2}]_{n_{LT}\times n_{LB}} & [0]_{n_{LT}\times n_B} & [0]_{n_{LT}\times n_I} \\ [0]_{n_{RT}\times n_L} & [\boldsymbol{I}e^{-(\xi_1+\xi_2)}]_{n_{RT}\times n_{LB}} & [0]_{n_{RT}\times n_B} & [0]_{n_{RT}\times n_I} \\ [0]_{n_{RB}\times n_L} & [\boldsymbol{I}e^{-\xi_1}]_{n_{RB}\times n_{LB}} & [0]_{n_{RB}\times n_B} & [0]_{n_{RB}\times n_I} \\ [0]_{n_T\times n_L} & [0]_{n_T\times n_{LB}} & [\boldsymbol{I}e^{-\xi_2}]_{n_T\times n_B} & [0]_{n_T\times n_I} \end{bmatrix} \begin{Bmatrix} \boldsymbol{u}_L \\ \boldsymbol{u}_{LB} \\ \boldsymbol{u}_B \\ \boldsymbol{u}_I \end{Bmatrix}.$$

Then, the equation of motion

$$(\mathbf{K} - \omega^2\mathbf{M})\{\boldsymbol{u}\} = \{0\} \tag{2.12}$$

can be written

$$\boldsymbol{W}^{\mathrm{H}}(\mathbf{K} - \omega^2\mathbf{M})\boldsymbol{W}\{\boldsymbol{u}_r\} = \{0\}. \tag{2.13}$$

which has been also pre-multiplied by the hermitian of $\boldsymbol{W}$, namely its complex conjugate. If now one defines two reduced mass and stiffness matrices $[\mathbf{M}_r]_{m\times m}$ and $[\mathbf{K}_r]_{m\times m}$ as

$$\begin{aligned} \mathbf{M}_r &= \boldsymbol{W}^{\mathrm{H}}\mathbf{M}\boldsymbol{W} \\ \mathbf{K}_r &= \boldsymbol{W}^{\mathrm{H}}\mathbf{K}\boldsymbol{W}, \end{aligned} \tag{2.14}$$

the harmonic equation of (2.12) becomes

$$(\mathbf{K}_r - \omega^2\mathbf{M}_r)\{\boldsymbol{u}_r\} = \{0\}. \tag{2.15}$$

Since $\boldsymbol{W}$ is a function of the wavevector in the reciprocal basis, it is possible to solve an eigenvalue problem for each couple (ξ_1, ξ_2):

$$(\mathbf{K}_r - \omega^2\mathbf{M}_r)\{\Psi_r\} = \{0\}. \tag{2.16}$$

The eigenvalues derived from equation (2.16) for each wavevector are put together to build the *dispersion surfaces*, which will be the topic of the next section since it is worth to first illustrate the implications of this procedure. It is common to say that, when the reduction of equation (2.11) is employed, periodic boundary conditions have been applied, meaning that the information of the infinite and periodic lattice have been added to the model; this is true although the way this happens is actually indirect. Indeed, the reduction constrains some of the edges to displace in the same way of their opposite edge, but with a phase shift given by the ratio between the periodicity and the wavelength. Thus, as the wavelength varies, the phase shift does the same. What it is imposed in this way is the consistency of displacements of opposite edges with a wave traveling across the unit cell, although no spatial periodicity has been explicitly assigned. This information is contained in the imposed wave itself: indeed, the condition expressed by the reduction can be true only if a plane wave travels undisturbed and this happens in the lattice when no reflection or scattering occur. Thus, the wave is traveling into a medium whose properties never change and, of course, that never ends. In this way, both the lack of boundaries and the periodicity are added to the model. Furthermore, this explains how a tool usually employed for stationary applications as the modal analysis can provide information about transient phenomena like wave propagation.

2.4 Results from unit cell analysis

2.4.1 Dispersion surfaces

Thanks to the application of Bloch's conditions to the unit cell, the phononic characterization of an infinite lattice has been reduced to the solution of an eigenvalue problem for each point of the (ξ_1, ξ_2) domain. Since this solution will be periodic in this domain, it is enough to take the (ξ_1, ξ_2) couples belonging to the first Brillouin zone. As in any dynamic problem, eigenvectors represent mode shapes and eigenvalues the square of frequencies, but unlike vibration steady state cases, in which these are resonance frequencies, for wave propagation they represent the frequencies of modes whose wavenumber is $\boldsymbol{k} = \xi_1 \boldsymbol{b}_1 + \xi_2 \boldsymbol{b}_2$. All the surfaces $\omega(\xi_1, \xi_2)$ obtained related to each mode are called dispersion surfaces or phase constant surfaces. Figure 2.4 shows the first eight for the studied geometry.

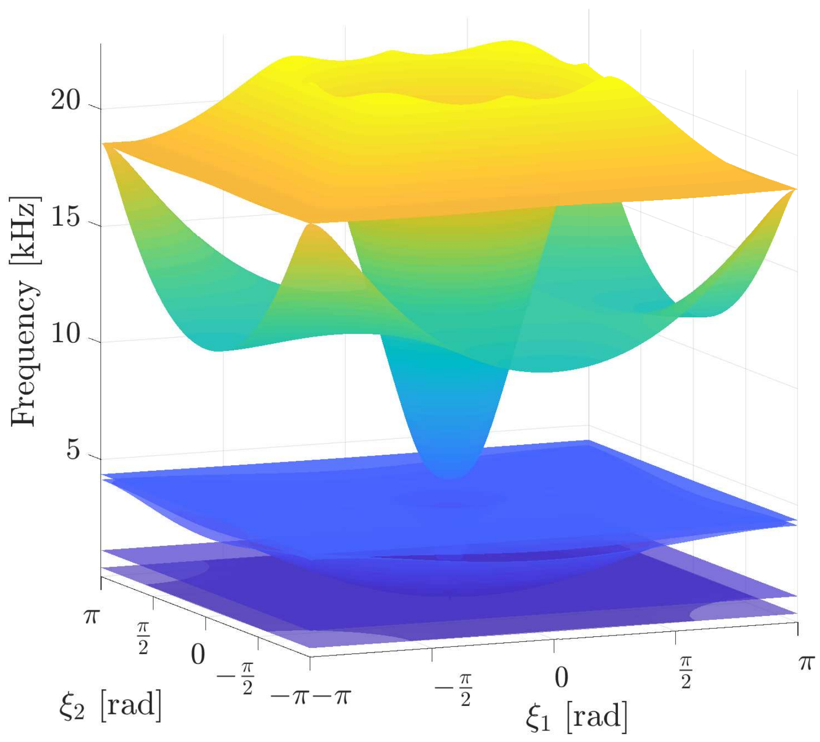

Figure 2.4: Lower eight dispersion surfaces in the first Brillouin zone.

All the features and properties regarding phononic processes are somehow depicted by these surfaces or by other plots of them, like the *iso-frequency contours* or the band diagrams, that will be illustrated later. Indeed, the shape of these surfaces affects velocity properties in different directions and at different frequencies, as these only depend on relations between frequency and wavenumber. Also band gaps can be detected from the analysis of these results, seeking for frequencies not involved by any mode.

Considering the whole set of modes, or at least a generous amount, it would be possible to see how this modes tend to group at some frequency bands rather than others, allowing to define a *density of modes* through which several material properties are described. For phononic applications, solid state physics addresses this density of modes, or better *density of states*, as a measure of thermal conductivity and this is reasonable since temperature is a description of vibrating particles. If, instead, these surfaces represent the eigenstates of the Hamiltonian in Schrödinger's equation for quantuum mechanics, the density of states describes the available energy levels of electronic orbitals in crystals and the positions of these bands with respect to the *Fermi Level* distinguishes conductors (metals) from insulators. Looking at these surfaces with the idea of available energy states can lead to a deeper understanding also of acoustic applications. However, none of these concepts will be investigated in this work as the attention will be focused only on the lower surfaces.

It can be already noticed looking at the (ξ_1, ξ_2) axes in Figure 2.4 that the limits of the first Brillouin zone are $-\pi$ and π: indeed, matrix $\boldsymbol{W}$ in (2.11) has a period of 2π in the reciprocal lattice and this information is carried in the eigenvalue problem in (2.16). It is easy to get a graphical proof of this periodicity looking at the iso-frequency contours, which are representations of dispersion surfaces by level curves. Figure 2.5 shows the contours of the first surface for the chosen unit cell, for wavevectors going from -3π to 3π along both directions. Due to the square arrangement, reciprocal lattice vectors and direct lattice ones are both parallel to the directions given by the cartesian reference frame. This allows these plots to have an immediate physical meaning, while for different kinds of arrangements it would be necessary to transform the surfaces from the reciprocal basis to the direct one. In Figure 2.5 also the first Brillioun Zone and its irreducible portion are represented; the latter can be obtained with a graphical construction that Brillouin explains in its book starting from the former. For a square lattice, the coordinates of the vertices of the shown irreducible Brillouin zone are O(0,0), A$(0, \pi)$, B(π, π), although it has to be understood that all the irreducible portions contain the information to describe the whole infinite lattice and they are as many as the double of the number of symmetry axes. The vertices of this area are said to be high-symmetry point and they are called critical points. Their denomination its not fixed and, in fact, both in solid state physics and in crystallography they are called Γ, M and K respectively.

2.4.2 Band structure

Despite a lack of a rigorous demonstration, it has been always seen that maxima and minima of the dispersion surfaces lie on the contour of the irreducible Brillouin

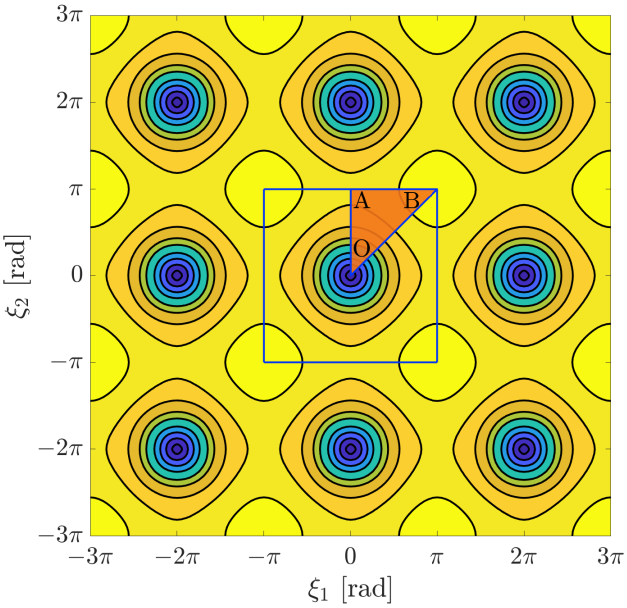

Figure 2.5: Contour plot of the first dispersion surface for the considered geometry showing the periodicity of the dispersion relation.

zone, so that for certain analysis, as for a band gap characterization, it is possible to define a coordinate s varying only along this contour. The plot of a set of dispersion surfaces along this domain is called band diagram or band structure, and it is the most straight-forward representation of the results from Bloch analysis. Figure 2.6 shows the band structure for the studied unit cell, in which the first eight modes are represented.

To really understand this plot it is necessary to fully understand the meaning of the s coordinate on the abscissa: in fact, one should think to a set of vector starting from the origin O and pointing at the position individuated by s; these are indeed wavevectors spanning the irreducible Brillouin zone contour. For this reason, in the OA section the growing of s means an increasing of the wavevector modulus while its direction stays parallel to one of the reciprocal lattice vector; in the AB section the wavevector experience a very little change in modulus while its direction rotate from one boundary of the irreducible Brillouin zone to the other; eventually, the wavevector reduce staying parallel to the BO segment. As the s coordinate approach the point O wavelengths grow since the wavevectors tend to zero. Some of the modes present a long-wavelength limit, meaning that their frequency tends to zero together with the wavenumber; these modes are called *acoustic* while the other ones are indicated as *optical*.

According to what has been said above, the lack of modes in the frequency range 4,5 ÷ 5kHz in Figure 2.6 testifies to the presence of a full band gap, meaning

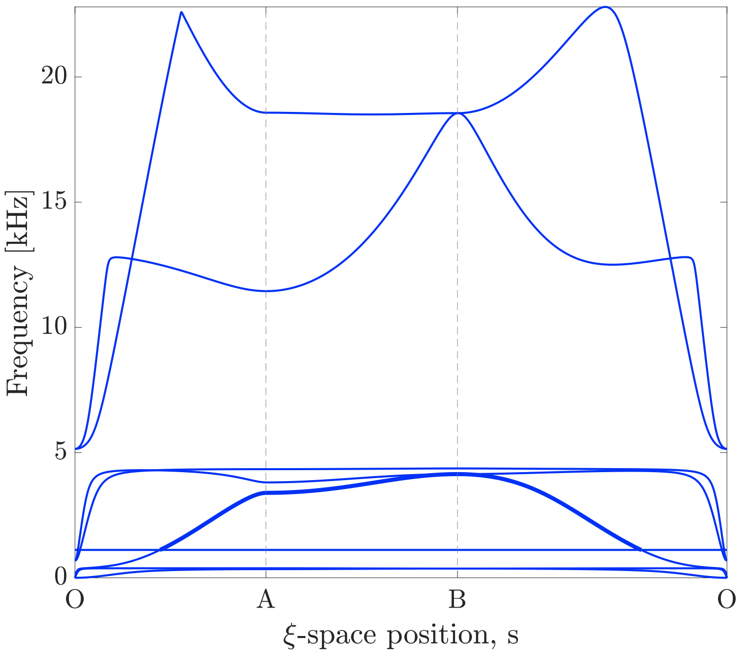

Figure 2.6: Band structure with the first seven modes for the considered geometry.

that the transmission is prevented for any kind of wave. Since each branch is a one-dimensional portion of a dispersion surface, each of them corresponds to a mode. Nevertheless, mode shapes are derived for each value of s, so that the mode can manifest with different mode shapes along the branch. Indeed, mode shapes are affected by the wavenubmer since they show how the unit cell behaves when invested by different wavelengths. Thus, once the excitation is given, only modes compatible with that excitation should be taken into account; in this way selective band gaps can be defined, meaning frequency ranges at which only certain waves are forbidden.

Before showing the mode shapes of the structure, it is worth to add a clarification: once obtained, modes are sorted in ascending order so that the n-th surface is actually the set of all the n-th eigenvalue calculated for each wavevector. Nevertheless, modes can change their relative order meaning that, if for some wavelengths a mode has a frequency lower than another, the opposite can happen for different wavelengths. This is detectable because some branches abruptly deviate just before crossing other ones. This is usually called *veering* and it does not have a physical meaning, it is just the effect of a misplacement of the modes, but must me known when looking to the surfaces to derive properties. The highest branch in Figure 2.6, for example, has two sharp corners out of which the slope of the surface drastically changes: they are two different modes whose eigenvalues happen to be the eight for different wavevectors.

2.4.3 Mode shapes

Figure 2.7 shows the first eight mode shapes evaluated at the critical point A: the wavevector is as long as the edge of the of the unit cell, namely the periodicity of the structure, and is directed along the ξ_2 axis, which is parallel to the y-axis. This means that the objects of the study are the ways the unit cell can store energy when waves of different nature, but with the same wavelength, are transmitted. Due to the different nature of the waves, meaning different mode shapes, some of them require more energy to be activated and this results in higher frequencies.

The first mode shape in Figure 2.7(a) belongs to an acoustic mode involving mostly the pillar and its first bending mode in the Y-Z plane; this oscillation is coherent with the propagation of the wave along the y-axis. The second mode in Figure 2.7(b) is of the same nature of the first but the bending of the pillar happens in the X-Z plane perpendicular to the wave: for this reason it requires an higher energy and lives at a frequency slightly higher than the first mode. Von Mises stresses represented by colors give a proof of these assumptions: in the first case most of the stresses are concentrated at the base of the stem along the y direction since all motion are in this direction. In the latter case the motion of the pillar is perpendicular to the wave and stresses in the plate distribute at the four corners. The third mode in Figure 2.7(c), likewise the former two, involves only the pillar which is twisted with a correspondent growing of the head diameter. Despite this exists, it is very hard to excite such a peculiar motion and no further discussions will be done about this. The fourth mode, depicted in Figure 2.7(d), is the first involving a consistent bending of the underlying plate. It is compatible with an out-of-plane wave along the y-axis. The stresses are greater in the plate as the pillar does not experience any bending, stretching or torsion and so does not participate to the energy storage. Since the prescribed excitation in our test will be out-of-plane, this existence of this mode and its characteristics will be leading parameters in the next analysis. The fifth and the sixth modes in Figure 2.7(e) and 2.7(f) could be seen as the second bending mode of the pillar. For both of them stresses are highly concentrated at the top fillet, just beneath the head: the difference, similarly to the case of the first and the second modes, is given by the enhancing effect of the wave when the bending happens in the Y-Z plane, parallel to the wavevector. The motion of the plate, indeed, decrease the energy needed to obtain that bending. The seventh mode in Figure 2.7(g) prescribes great displacements to the plate, again compatible with an out-of-plane excitation carried by a wave lying on the y-axis. The relative bending between the stem and both the head and the plate is considerable and leads to the hypothesis that the role of the plate is crucial to the point that the correspondent mode involving motion in the X-Z plane can not be energized but at very high frequencies. Eventually, in Figure 2.7(h) the eighth mode is illustrated. It is again compatible with an out-of-plane mode along the y direction and looks similar to the fourh mode in Figure 2.7(d), although here the energy is mostly exploited in the stretching and compression of the stem, while the head plays a secondary role. Figure 2.7(d) and 2.7(h) also highlight how the wave taken into account has a wavelength the double of the cell edge, as in both cases the plate bends following an half-wave shape.

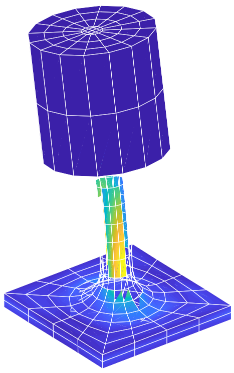

(a) 346 Hz

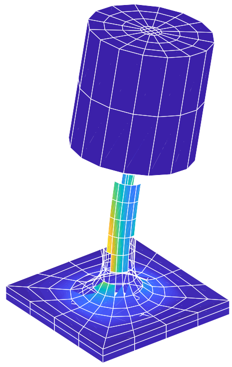

(b) 382 Hz

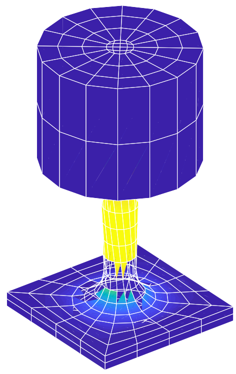

(c) 1114 Hz

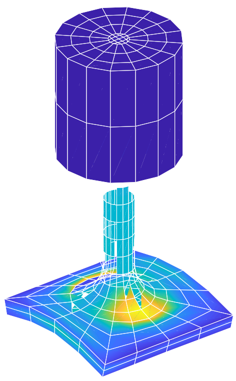

(d) 3393 Hz

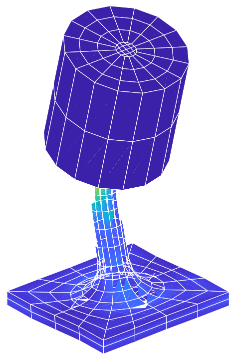

(e) 3809 Hz

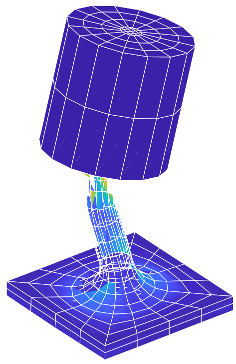

(f) 4338 Hz

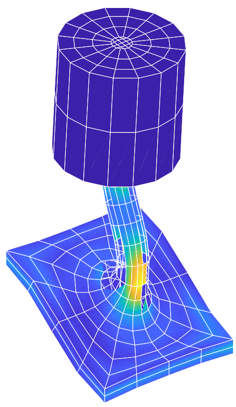

(g) 11448 Hz

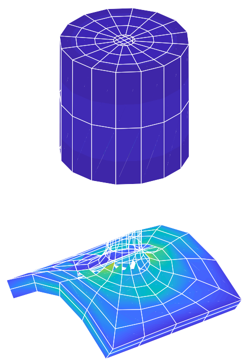

(h) 18573 Hz

Figure 2.7: Lowest eight mode shapes evaluated in the critical point A with Von Mises stresses represented by colors and normalized against the maximum on the surface. Captions display the frequency of each mode.

2.4.4 Velocities

While the presence, or lack thereof, of dispersion surfaces in certain frequency ranges addresses for band gap behavior, information about velocities can be derived from the shape of surfaces. To model wave propagation, two different velocities are usually employed, both depending only on the relation between frequency ω and wavevector $\boldsymbol{k}$. The phase velocity

$$\boldsymbol{c}_p = \frac{\omega}{|\boldsymbol{k}|}\hat{\boldsymbol{k}} \tag{2.17}$$

relates the wavelength to the time in which a point of constant phase, as a crest, takes to cover it. Since it is simply the ratio between the frequency and the modulus of the wave number, a quick outlook of the directionality is given by iso-frequency contours of the dispersion surfaces. In this case, indeed, the numerator will be constant and the phase velocity will be greater for points closer to the origin, and vice-versa; for an isotropic media these contours would be circular. In periodic structures, the axial-symmetry of the arrangement usually plays a role in determining these properties. To deliver some clarifying examples, iso-frequency contours of the first eight surfaces are shown in Figure 2.8.

Veering, namely the switch of position of two modes when their frequencies approach, should be taken into account when looking at these plots: the fourth mode, for instance, shows a flat low frequency region which actually belongs to the third mode: this becomes clear looking at the fourth branch of the band structure in Figure 2.6, in the intervals close to the origin O. In the same way, the seventh mode has a steep region close to the origin of the reciprocal lattice space which correspond to an axial mode, differently from the one depicted in Figure 2.7(g). In Figure 2.8, to avoid misunderstandings and wrong conclusions, areas corresponding to modes different from the main modes of the surfaces has been cut. Through a painstaking manipulation of results it would have been possible to reconstruct the original physical surfaces.

The first dispersion surface in Figure 2.7(a) provides a good example of frequency dependent directionality: albeit looking only at these contours is not sufficient to determine this property, the change of their shape is an initial trace of it. The second-last contour showed has a squarish shape that should lead to anisotropic propagation for that frequency: likewise what explained above, since the same frequency, i.e. the contour level, is divided by wavevectors of different lengths, as the contour different from a circle, phase velocity will not be equal in all the directions. The second surface of Figure 2.7(b) present some strongly anisotropic features although the frequency range spanned by those contours is extremely narrow ($368 \div 381$ Hz). The third surface in Figure 2.7(c) describes a completely flat mode, as depicted by Figure 2.6; further examination will be carried on this mode when group velocity will be presented. Contours of the fourth surface in Figure 2.7(d) are mostly circular but the higher two, which are not closed lines, at least looking at a

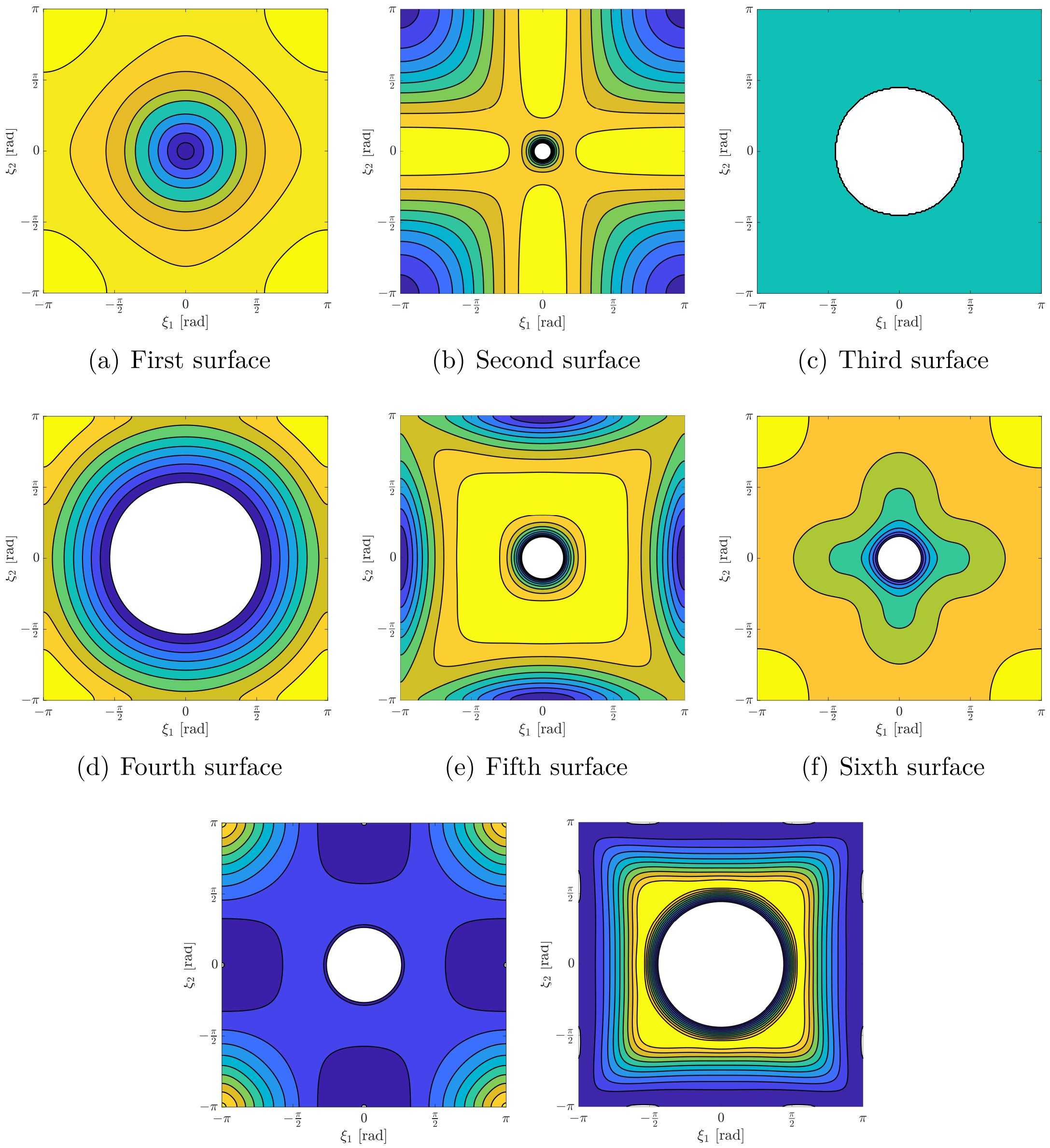

Figure 2.8: Iso-frequency contours plots of first eight dispersion surfaces in the first Brillouin zone. Effects of veering on these representations have been canceled cutting areas related to modes different from main ones. Color scales span each surface interval.

single Brillouin zone. All the remaining surfaces show strongly anisotropic shapes: some of them also reveal a concavity that changes along different directions, like in Figure 2.7(e). This characteristic plays an important role for the derivation of group velocities.

Group velocity is defined as the gradient of dispersion relation

$$\boldsymbol{c}_g^{\mathcal{I}} = \nabla(\omega(\boldsymbol{k}^{\mathcal{I}})) = \left(\frac{\partial\omega(\boldsymbol{k}^{\mathcal{E}})}{\partial k_1}, \frac{\partial\omega(\boldsymbol{k}^{\mathcal{E}})}{\partial k_2}\right) = \left(\frac{\partial\omega(\boldsymbol{k}^{\mathcal{B}})}{\partial \xi_1}, \frac{\partial\omega(\boldsymbol{k}^{\mathcal{B}})}{\partial \xi_2}\right), \tag{2.18}$$

in which the equivalence between all the basis is due to the proportional relations connecting them: as the surfaces enlarge, axes do the same and vice-versa so that the derivative doesn't change. The same can not be said about phase velocity, since frequencies values are not different among basis. Group velocity plays a more relevant role than phase velocity because it contains information about the energy propagation. Its physical meaning, indeed, is the velocity of propagation of the envelope of a wave packet, also referred as burst, obtained exciting in a narrow frequency band. Figure 2.9 provides an example of a wave packet and its envelope, the orange dashed line.

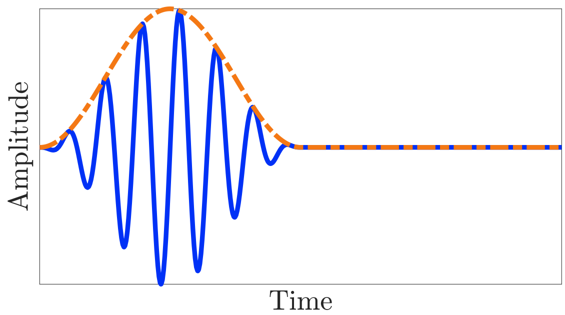

Figure 2.9: Example of a wave packet.

Comparing equation (2.17) and equation (2.18) it is clear that if the frequency was a linear function of the wavevector, group velocity and phase velocity would be the same and they would not change for different frequencies. This is what happens, in general, at the long-wavelength limit and in non-dispersive media, whose dispersion surfaces for two-dimensional structures are semi-cones. The band diagram of Figure 2.6 allows both to evaluate this derivative along one dimension at a time and to compare it to the line connecting the origin and the selected point, whose slope represents phase velocity. In the OA section, acoustic modes evaluated at very low wavevectors are non-dispersive. When the wavevector grows, branches fold and the difference between the two velocities grows as well: both diminish as an effect of folding although group velocity in more sensitive to this. When branches become flat, group velocity is null and the propagation of that mode is forbidden. Since it has been said that also real wavevectors prevent waves from propagating, it should be reminded that, in the case of null group velocity, energy keeps its mechanical nature being only confined.

Iso-frequency contours become even more relevant in the evaluation of group velocity: since this is the gradient of dispersion surfaces, its direction will always be perpendicular to these contours. Once the gradient for each contour point has been evaluated, the collection of all the gradient vectors moved to the origin of the reference frame allows to visualize the group velocity in each direction. Therefore, if a contour shows a change of its concavity, like the second-last contour of Figure 2.8(f), group velocity plot will display lobes in its shape. As said before, group velocity directionality is much more relevant than phase velocity one since the energy of the wave packet travel with its envelope.

Figure 2.10 contains group and phase velocities plots for the first, the fourth and the sixth modes. Phase velocity plots are presented on the left column while group velocity plots on the right one. For each mode three frequencies have been chosen and it is possible to read them in contours legend. These modes have been chosen as they deliver different examples worth to examine in depth.

The three contours showed for the first mode are all characterized by outward-directed arrows, which represent the expected behavior of dispersion relations moving away from the origin. The two lower contours are circular and the arrows on each of them are of the same length. Therefore, both their group velocities and their phase velocities keep a round shape, meaning that those frequencies propagate with isotropic patterns. The outermost contour, which is also higher in frequency and belongs to the folded portion of the first mode, has a squarish outline and the gradients are not equal everywhere. As it has been said above, phase velocity is affected only by the shape of the contour in a way that outer points will have a smaller velocity; Figure 2.10(a) confirms this as his yellow set of points promote the directions along which the third contour is closer to the origin. Imaging to make all the gradient arrows start from the origin, one would obtain the group velocity plot on the right column marking the tips of arrows. As the higher frequency gradients are not equal in modulus, the group velocity shows directionality although velocities are way smaller than the lower frequency ones. As clarified in the caption, arrows are scaled to avoid superimposition so their length is consistent within a contour but it is not between different contours.

Similar considerations could be made for the fourth mode depicted on the second row. Again, lower frequencies propagate without showing particular any preferred direction. In this case the third contour not only lacks of a round shape, but it does not exist at all along some directions. The most direct effect is on the phase velocity which, likewise the contours, is almost constant along each direction it exist. At the extremity of this contour branches, the concavity slightly changes so that the gradients are not all radial. This variation is enough to generate lobes like the ones of Figure 2.10(f). The numerical simulation of propagation transient will be carried out only to show the directionality of this frequency and will not be object of experimental test.

Eventually, the sixth mode has been chosen for the shape of its middle contour, whose strong change of concavity along different directions provides a more clear example of what has been said for the former mode about group velocity. The difference between principal directions and diagonals increase as the frequency grows, so that the squarish features of the lower mode are enhanced. For this reason the blue group velocity plot in Figure 2.10(i) modifies up to show lobes like the red plot does. However, these are short, wide lobes that encompasses almost all directions. Likewise the first mode, velocities at higher frequencies become very small. Phase velocity plots show once again how this property is affected by contours shapes.

2.5 Summary

Due to the length of the chapter, this section provides a brief summary of the encompassed topics. At first it has been presented how the lattice is described introducing, along with the cartesian reference frame, the direct lattice basis and the reciprocal lattice one. Thereafter, fundamental tools for Bloch's analysis have been demonstrated and periodic boundary conditions have been applied to a three-dimensional finite element model of the unit cell. Such conditions take into account the wavevector to evaluate the phase shift across the unit cell. Therefore, the solution of a reduced eigenvalue problem can be found for each value of the the wavevector. The relation between the frequencies, found as eigenvalues, and the wavevector, is shown to be periodic in the reciprocal lattice basis. Later, it has been explained how focusing only on the contour of this reduced portion of the reciprocal lattice space it is possible to build the band structure of the lattice. The properties of this representation have been clarified together with the illustration of the mode shapes that it describes. At last, phase and group velocities have been defined and qualitatively derived from the iso-frequency contour plots presented in the same section.

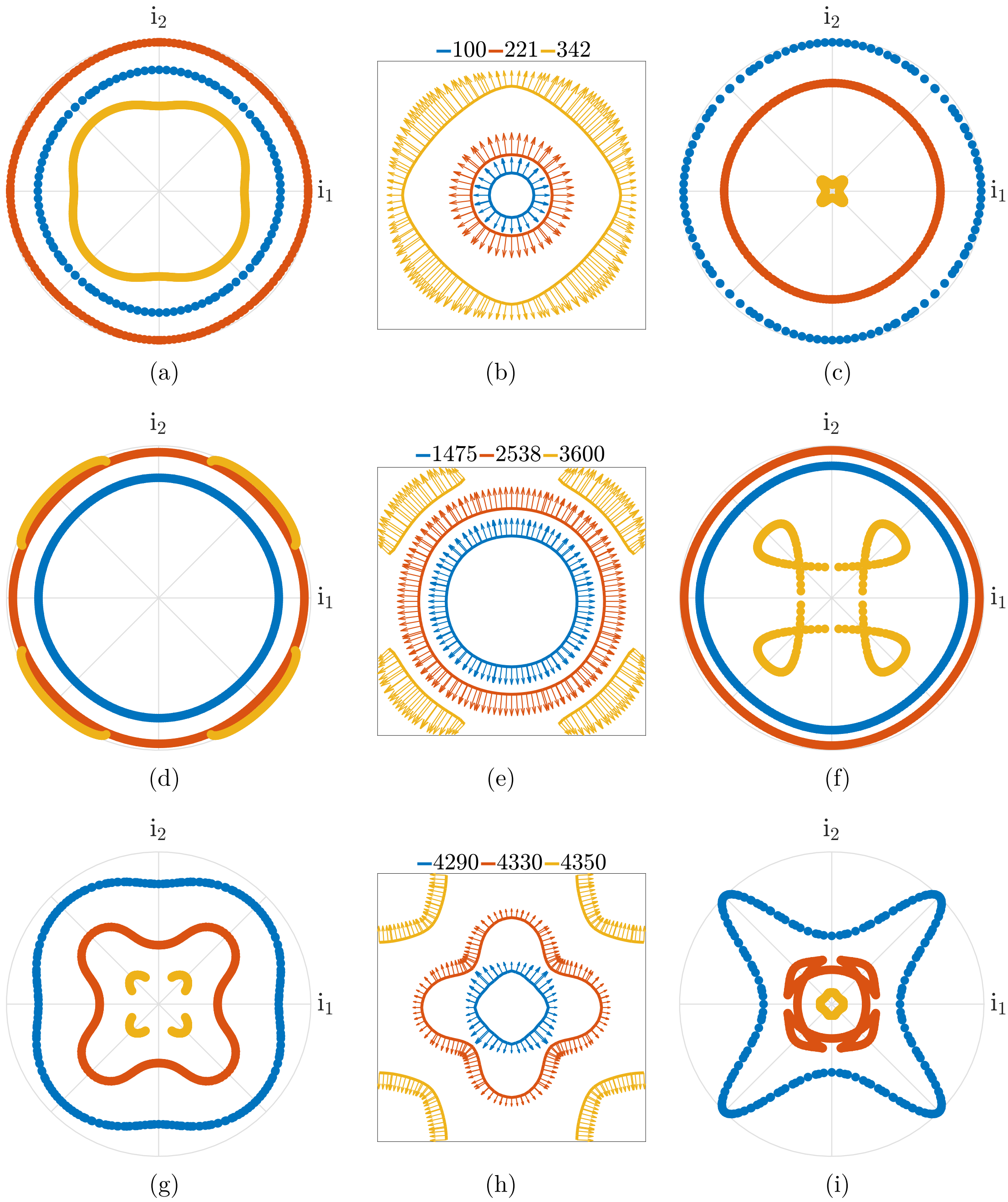

Figure 2.10: Phase velocities (a, d, g), iso-frequency contours equipped with gradient arrows (b, e, h) and group velocities (c, f, i) for the first, the fourth and the sixth modes, respectively. Contour legends are expressed in Hz and apply for each row. Gradient arrows are scaled to prevent superimposition.

Chapter 3

Finite dimensions lattice

As aforementioned, the predictions given in the previous section could not have been derived without looking at the behavior of the lattice effectively excited. Indeed, the knowledge gained about band gaps and the characterization of their nature have been results of mostly full scale analysis. Here lies the first, main, and inevitable source of discrepancy with Bloch analysis since there is no possibility nor real meaning to either observe or simulate an infinite lattice. Hence, the study is pointed to finite dimensions lattices whose agreement with theoretical results depends on how well the periodicity is replicated. This means that even small structures can mimic infinite repetitions although common magnitudes for velocities do not permit to observe wave propagation in the very little time before waves reach edges.

In this section all the results from both numerical and experimental test will be provided and compared, as they will be shown to agree with the unit cell analysis and eventually to match each other. At first, steady state analysis will be provided as experiments have been carried out only for this application; at the end of the chapter, instead, only numerical simulations will be shown to validate those properties that can only be taken into account with transient analysis, like velocities.

Before presenting the results, an outline of the design process is given in the next sections, regarding first the unit cell and then the whole specimen. Also, a brief description of the experimental setup will be given.

3.1 Design

The introduction of this work ends with the sketch of the unit cell in Figure 1.3 although no information have been given about the design process. The purpose of this section is to provide an idea of the issues that have been encountered, related to the manufacture process and the phonoinc performance of the specimen. As the former implies the design of the specimen over the unit cell, some pictures of earlier plates are given in this chapter to unfold the manufacture issues, although more information about their arrangement are provided in the next section.

The cornerstone of the design has been the choice of a stubbed plate as object of the study. This kind of structures has been widely analyzed for locally resonant phononic crystal applications, finding its main feature in the continuity of the substrate: the plate, indeed, can be considered as an homogeneous medium, differently from the case of in-plane resonators. Furthermore, most of the works available at this time [1, 4, 19, 30] make use of specimens which are assemblies of different parts: in this work additive manufacturing allowed to test homogeneous single-pieces specimens. This leads to a more consistent mathematical model since it is hard to analytically predict the behavior of junctions, especially for such sensitive phenomena.

3.1.1 Phononic characteristics

Once the nature of the crystal has been chosen, some first attempts have been made starting from a primitive geometry, depicted in Figure 3.1, to understand which parameters influenced phononic processes. The feedback of this study are the results presented in the previous chapter, especially band structures and mode shapes. In other words, the aim has been to design the band structure itself improving the awareness of the relations between geometric and phononic parameters. Similar analysis have been carried on in [20, 22].

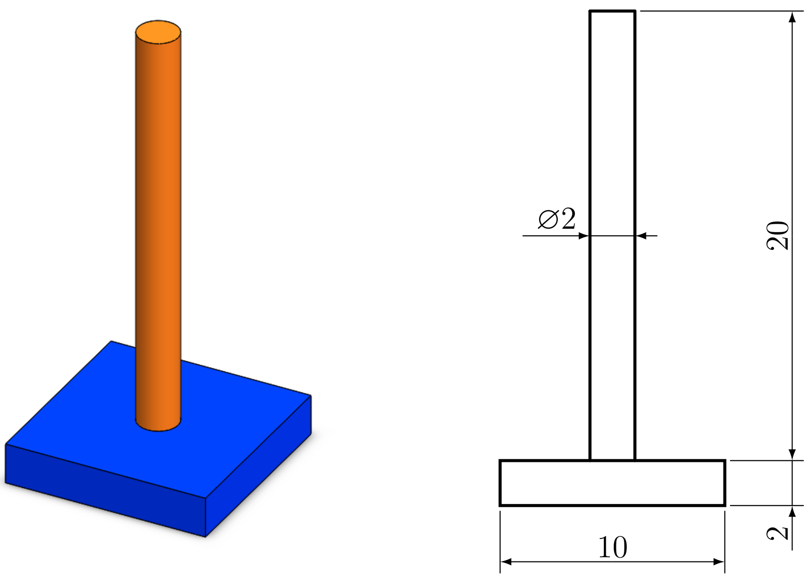

Figure 3.1: First attempt design of the unit cell.

At the beginning, the result sought looking at the band structure has been a sign of band gap that did not came out: all the lower branches in the band diagram intersected each other so that no frequency band was left free. At that time, there was not a full consciousness of the meaning of each branch and of the relations between geometric parameters and phononic features, so that several attempts have been made to build this knowledge. In the past, it has been observed how, selecting the maximum frequency of each mode, these corresponded to the resonance frequencies of the same modes when a modal analysis was carried on the resonator alone. Therefore the onset of any possible band gap will correspond to one of these maxima. Given this, one should know which branch to take into account to adjust the geometry in order to place the resonance frequency at the desired level. Naturally one can not modify a single mode without affecting all the others, so the process is always carried out by attempts and band gaps signs are those that suggest which branch should be analyzed.

First possibilities to open band gaps has been found lowering the resonance frequencies of both the plate and the pillar. The former has been seen to be more sensitive to its width, namely the periodicity, than to its thickness, although since additive manufacturing does not allow to have big specimens, it has been chosen to keep this value to a = 10mm in order to ensure space for a minimal repetition. Clearly, being able to act only on the plate thickness to lower the resonance frequencies, this has been diminished.

The design of the pillar has been the most challenging and important phase of the work. Despite the plate played a fundamental role in determining the order of magnitude of the eigenvalues, the shape of the pillar allows to tailor at a smaller scale the band structure. Looking at the resonator as a clamped beam, which is not but works for a first approximation, the opportunities to lower down the first resonance frequencies lie either in a longer pillar or in its weakening: both ideas aim to a stiffness reduction. Applying both the solutions, we obtained a full band gap with the geometry illustrated in Figure 3.2, whose band diagram is depicted in Figure 3.3(a).

The two main characteristics of this design are the very thin plate and the hollow pillar. The latter, in particular, has been thought as a way to decrease the stiffness without decreasing the mass. Figure 3.3(a) shows a *full* band gap in the frequency range 8,5 ÷ 10,5kHz: in this region there is no way for the unit cell to store energy, whatever the excitation is. The reason behind the attribute full to the band gap lies in this. The shaded orange region, instead, represents a *modal* band gap, a frequency region in which the capability of the unit cell to store energy depends on the excitation: if this is compatible with the mode shapes of the present branches, transmission is allowed.

There can be no certainty about the excitation decomposition through modes operated by the structure. Thus, numerical steady-state simulation of finite dimensions lattices are carried out to understand the response to the prescribed excitation and the results of this analysis are presented in the next chapter. Since it has been chosen to study the flexural behavior of the plate, out-of-plane excitation has been

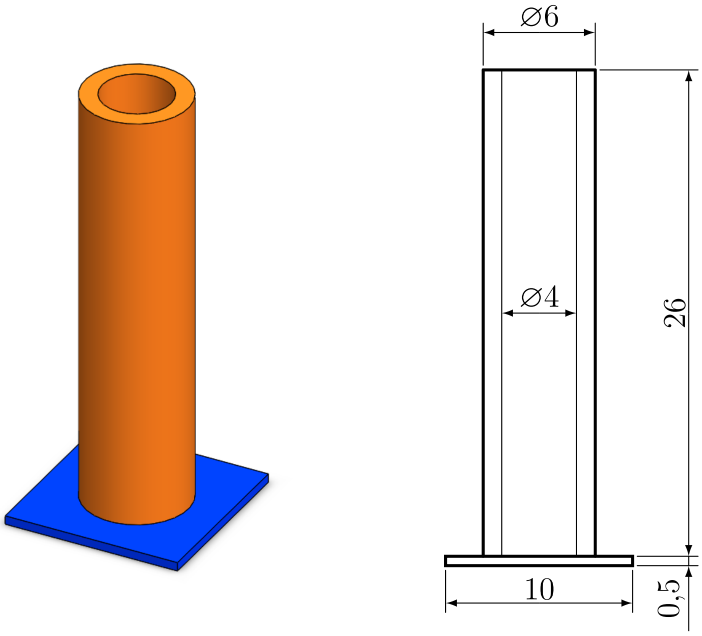

Figure 3.2: First unit cell employed for experimental tests.

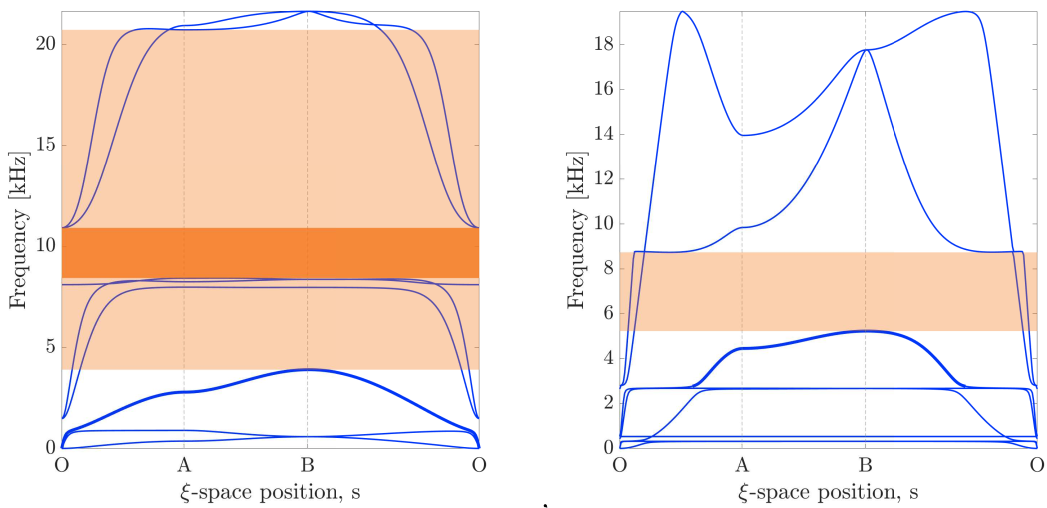

,

(a) Geometry: Figure 3.2

,

(b) Geometry: Figure 3.5

Figure 3.3: Band diagrams of the first two unit cell manufactured. The orange opaque band highlights a full band gap while the transparent bands a modal band gap. Stressed branches are the reference for flexural behavior.

investigated. In this way it has been understood how the third mode is the one to take into account when such an excitation is given. Therefore the onset of the modal band gap is identified by the maximum of the third branch.

The band gap of Figure 3.3(a) is very clear as his lower modes can be easily detected and it match the similar case proposed in [22]. Thus, this has been the first design to be manufactured and tested. Unfortunately, the very little thickness of the plate and the limited toughness of PolyJet materials led to the break of the specimen, first with a small crack due to the detaching of the shaker stinger, and eventually split in half during an attempt to stretch the plate, as shown in Figure 3.4.

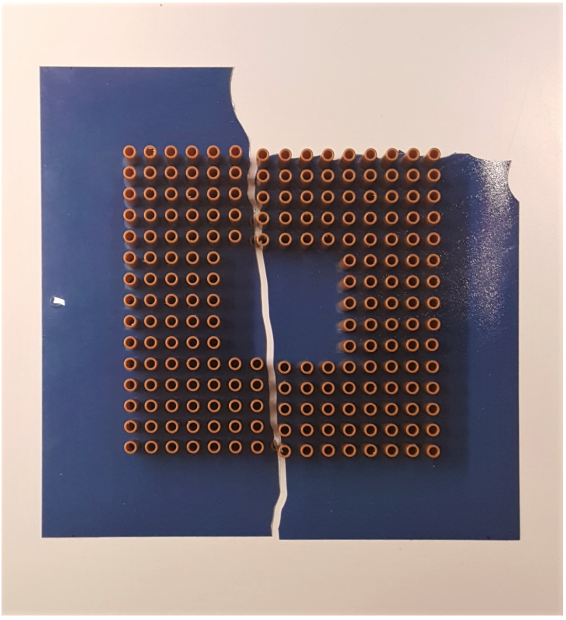

Figure 3.4: First specimen manufactured broken in two pieces. The vertical linear crack has been the effect of a stretching attempt, while the missing part has been removed to carry out some test on a plain plate.

To improve the strength of next specimens it has become necessary to increase the thickness up to one millimeter, although this forced to start from scratches the design of the pillar: indeed, an important role in the global stiffness for flexural excitation is played by the portion of the plate between the edge and the pillar, see Figure 2.7(d) at page 21, but the hollow geometry reduce this portion increasing stiffness and resonance frequencies.

In order to keep both a sufficient mass and enough plain plate for the reasons just unfolded, the mallet-like design in Figure 3.5 has been brought out. The big head increases the inertia for either flexural and axial behavior of the pillar and the same effects are given by the slender stem. The two band structures depicted in Figure 3.3 present a stressed branch describing the mode associated with a flexural behavior. Looking at Figure 3.3(b) one should consider veering effects and follow the steep slopes out of the stressed region. Despite the completely different design, the two branches look similar and their maxima are both close to 5kHz, indicating that the modification of the pillar compensated the thickness increase. Other branches, instead, albeit looking similar, appear at significantly different frequencies: it is the case of the flat mode just beneath the full band gap in Figure 3.3(a) that is positioned at very low frequencies in Figure 3.3(b). This is of the kind of Figure 2.7(c) at page 21, which represents a torsion of the pillar, so hard to energize to be of no interest. It is also worth notice that the band gap width of Figure 3.3(b) is much smaller than the previous design. The goodness of this property depends on the application; for the example that will be shown in the next chapter, a more narrow gap eases the identification of its limits. Of course, for filtering purposes the wider gap would be more effective.

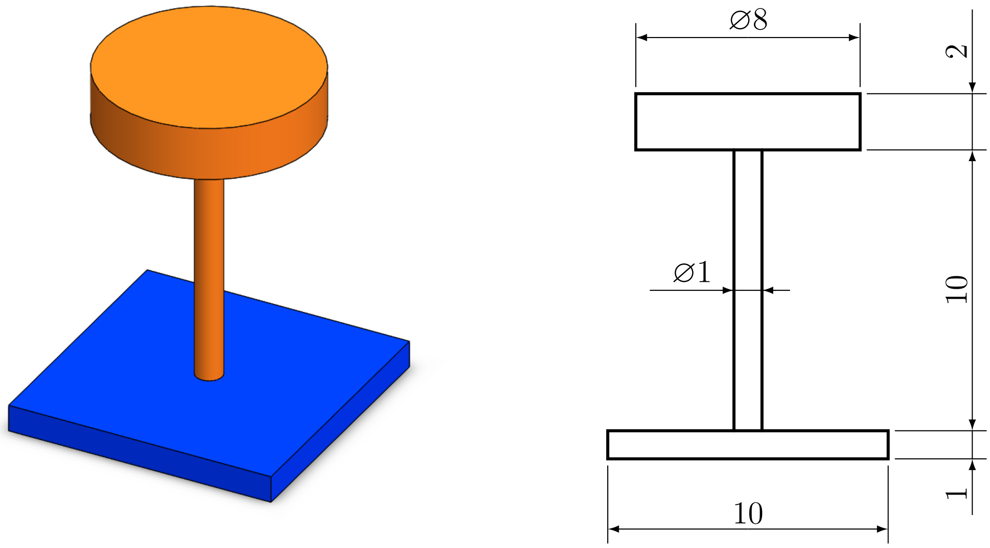

Figure 3.5: Second unit cell manufactured showing the mallet-like design.

3.1.2 Manufacturing aspects

At this point the desired phononic properties have been found and next updates concern manufacturing aspects. The design of Figure 3.3(b) requires the use of supports for the printing process. First specimens have been obtained employing standard support material that is removed mechanically; due to the great slenderness of the the resonators those broke at any attempt to clean the plate. Figure 3.6(a) shows the result of an attempt to remove supports carried out with a water jet.

Realized this, fillets have been added to the design to try to strengthen the structure and the supports material has been changed to a dissoluble one, the SUP-706. An example of a specimen before supports removal is shown in Figure 3.6(b). It should be reminded that the availability of this feature for additive manufacturing is achieved thanks to the state of the art machines of the *Earl E. Bakken Medical*

Device Center.

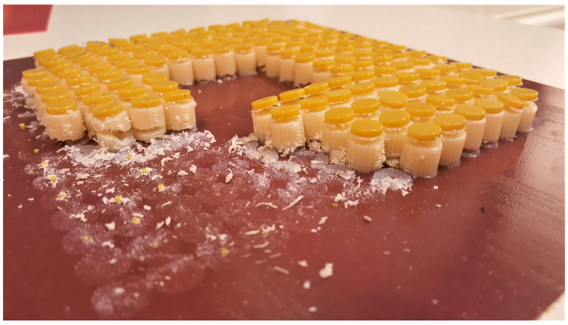

(a)

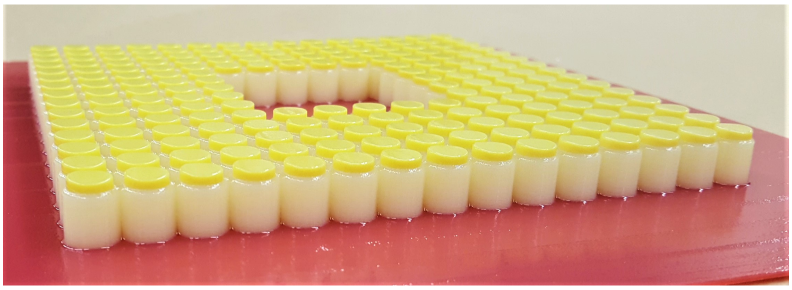

(b)

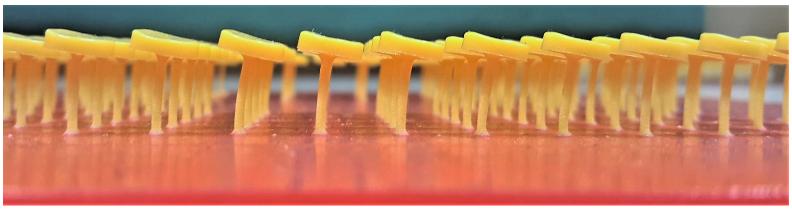

(c)

Figure 3.6: (a) Specimen employing mechanical removable supports with detached pillars due to a failed cleaning attempt made by means of a water jet. (b) Printed specimen before and after (c) dissolvable supports removal. Supports material is the white one surrounding pillars. The reference geometry is the one depicted in Figure 3.5.

The advantage of dissolvable supports is twofold: it prevents the operator from applying forces to the structure to remove supports and it allows to design complex geometries that require use of supports in zones that can not be reached manually. Once the printing has been done, parts have been soaked in a water bath containing 2w% sodium hydroxide and 1w% sodium metasilicate. This basic blend quickly dissolve supports for parts of bigger dimensions which do not present such small features. In this case the bath time is around one hour. For the geometry represented in Figure 3.5, due the minuteness of the details, the bath has been dilute and the soak carried on for two days. Comprehensibly, the expertise of the center does not encounter such detailed geometries, thus some attempts had to be made. Indeed, the first specimen manufactured with dissolvable supports, the one in Figure 3.6(b), has been shown to be sensitive to the soak time, which has been overestimated with a resulting weakening of the stems of the pillars culminated in their bend under the relatively heavy heads. An attempt to straighten resonators has given partial results visible in Figure 3.6(c).

Despite the addition of small fillets, such delicate pillars have come off the plate just being touched, jeopardizing the whole process. Nevertheless the phononic properties have not been particularly affected by this, so some perliminary test have been carried out with the specimen and suggested that smaller plates could have been more advisable due to the intrinsic damping of the material.

3.1.3 Final design

All the information collected during the design process led to the geometry presented in Figure 3.7, where the stem has a doubled diameter with respect to the one in Figure 3.5. When the diameter of a beam with circular section is doubled, its bending resistance grows eight times due to the existing cubic relation between these properties. The increased stiffness has been compensated with a bigger, heavier head, whose height is four times the former, although their diameters are the same. Of course, the aim of this operation is to keep the frequencies involved in phononic processes as low as possible. Eventually, also the radius of the fillets has been increased to two millimeters to ensure an adequate toughness, and this has shown to affect very little the dynamic behavior, namely the band structure.

Figure 3.8 shows the band diagram of the unit cell, already provided in Figure 2.6, although here the excitation has been chosen so it is possible to highlight the modal band gap for flexural waves. The maximum frequency of the band gap lies around 12kHz making hard to detect experimentally the recovery of transmission. The reasons behind this difficulty should be seek both in the laboratory equipment and in the material performances: about the former, it is reminded that the experimental setup will be presented in the next chapter, although it is possible to anticipate the presence of the shaker and its limitation for high frequency. The latter, instead, represents something foreseen and actually answer one of the questions that motivated this work. Vero® material, sort of a PLA, has been shown to work with acceptable performances for low frequencies, providing a moderate damping; nevertheless, when the frequency approaches the order of 10kHz the quality of the transmission decreases tremendously. In next chapter the damping influence has been modeled with a proportional damping method, although its characterization stopped at a qualitative level and would deserve a dedicated study; despite the drop of transmission at higher frequencies, additive manufacturing allowed the realization

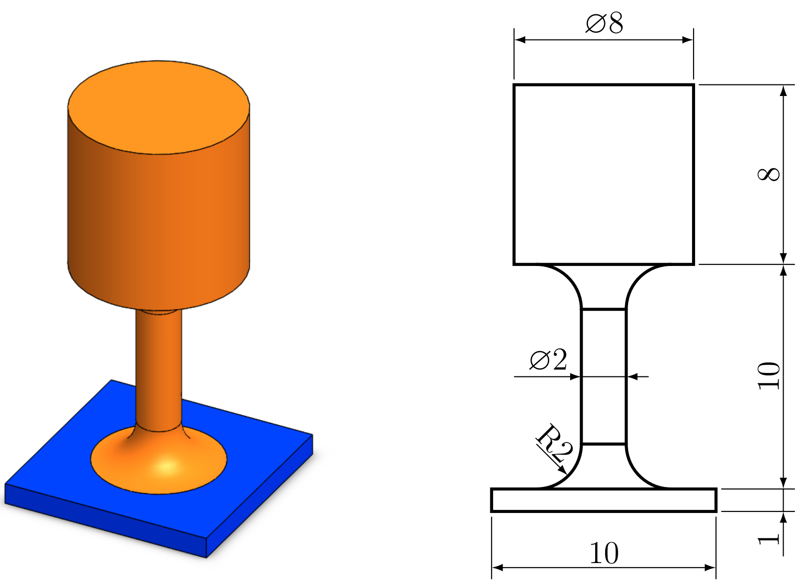

Figure 3.7: Definitive unit cell draw.

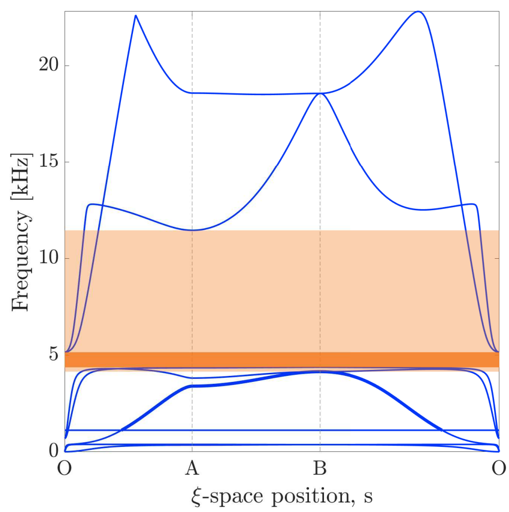

Figure 3.8: Band structure of the definitive geometry with highlighted band gaps.

of specimens whose terrific complexity would have been an impossible achievement with conventional technologies.

3.1.4 The specimen

Likewise the unit cell, the whole structure had to be thought facing limitations imposed by both performances and manufacturing; some pictures of first attempts have already been presented as the reciprocal influence between the designs of the whole structure and the single cell has been proven to be significant.

Two main arrangements has been taken into account and the first is the one proposed in the previous section, made of a square area populated by resonator, surrounded by a portion of plain plate. The pillar area is constituted by a 15x15 matrix of resonators showing a 5x5 hole in the middle, where hole indicates a lack of pillars, as the plate beneath is present. A schematic top view of the geometry is given in the left image in Figure 3.9.

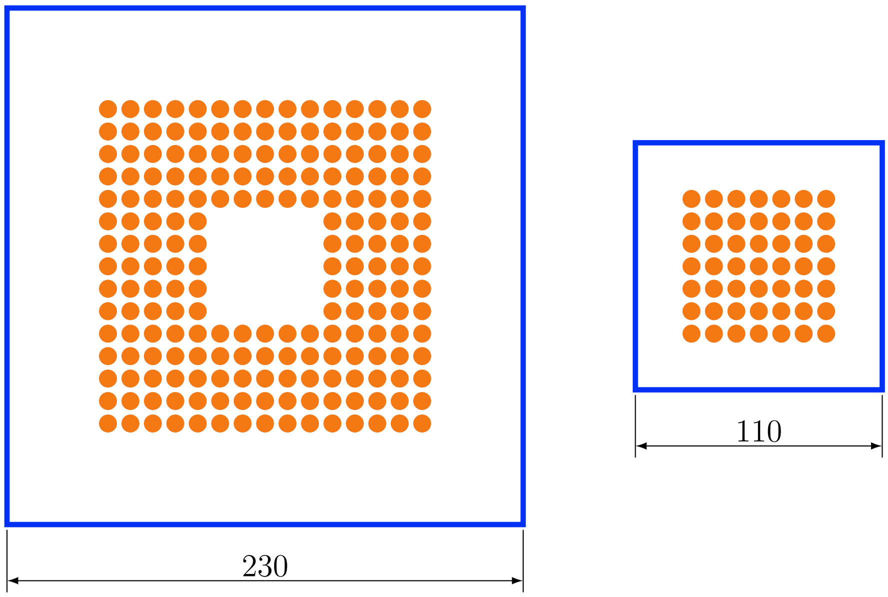

Figure 3.9: Schemes of the two kind of specimens. The first, larger one shows a square matrix of 15x15 resonators with a 5x5 hole in the middle. The smaller specimen is the definitive one and its full matrix of resonators is 7x7.

The idea behind this arrangement has been to create a fence between two portion of plain plate in order to show how waves of certain frequencies are not allow either to enter, if the excitation is provided in the outermost portion, nor to escape, in the opposite case. After earlier test with the plates shown in Figure 3.4 and Figure 3.6, it has become clear that the internal damping provided by the composite material would have not allowed much energy to be transferred to areas far from the excitation point. If the aim is to show how waves are stopped by resonators, the lack of these should ensure a sufficient transmission so to have a greater contrast. Also, the convenience of the arrangement has been re-thought since the excitation has been provided always from the outer portion during early test. Thus, the presence of the plain area in the middle of the plate had no real reason to exist.

Mainly for these two reasons, when the geometry of Figure 3.7 has been employed, the plate has been modified to the smaller one in Figure 3.9, whose matrix of resonators is full and its reduced dimensions let the energy acceptably reach opposite areas.

As anticipated, the increased toughness of the last specimen permitted an easier manufacturing that encountered no troubles. Some pictures of the specimen are shown in Figure 3.10.

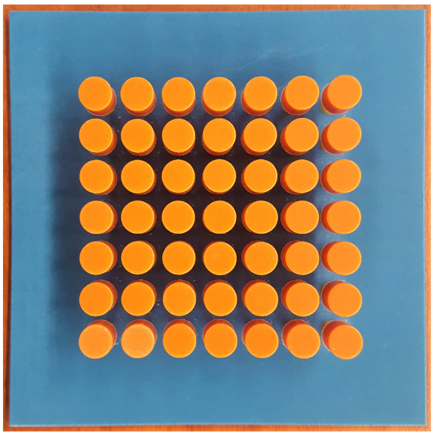

(a)

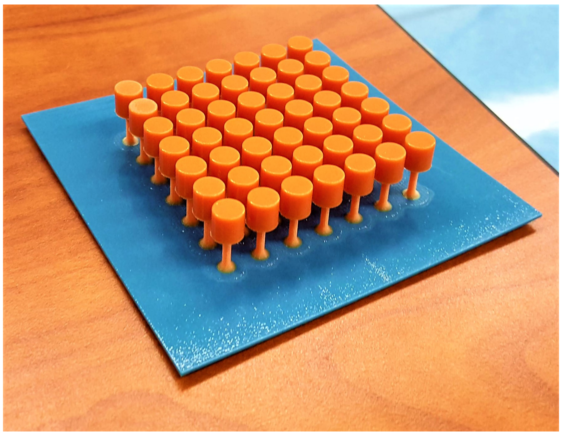

(b)

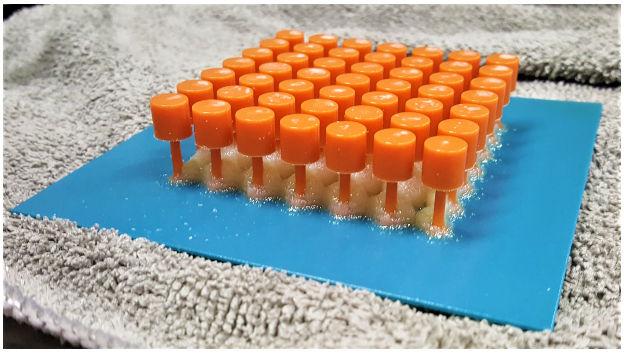

(c)

Figure 3.10: (a) and (b) views of the specimen. (c) Cleaning middle stage.

3.2 Numerical steady state simulation

Above, it has been said that the understanding of the mode shapes triggered by any excitation could not be fulfilled without a numerical simulation of the case, thus selecting both the excitation and the frequency. To do so it is not necessary to have a final design of the specimen, as the object described by the band structure is an infinite lattice. Nevertheless, it is convenient to carry out numerical simulations of the experimental test to understand what to expect. This section will show the result of this investigation after a brief presentation of the dynamic FE model considered.

It should be underlined right away that, despite the band diagram describes wave propagation, the proposed simulations refer to steady state analysis. The link between the transient analysis of a propagating wave and the steady state case has not been fully clarified yet. It can be certainly said that after the wave interacts with the domain borders it is reflected and it is summed to the incoming wave. Eventually, all the components are summed and the resulting displacement field is that given by Equation (3.2). Nevertheless, Bloch analysis does not contemplate any of this mechanisms and the ways in which the characteristics of the infinite lattice affect the finite structure should be better investigated.

3.2.1 FE model of the specimen

As for the unit cell, a three-dimensional finite element model employing eight-nodes hexaedra elements has been assembled to analyze the dynamic behavior of the plate. The mesh that has been used is depicted in Figure 3.11.

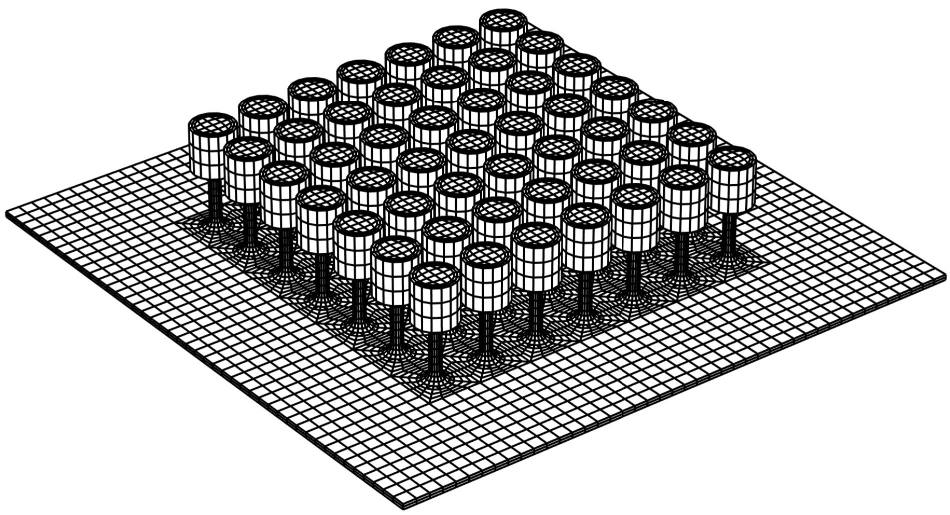

Figure 3.11: Mesh of the specimen.

The assembly of mass and stiffness matrices followed the same procedure used for the unit cell, although the dimensions of the problem are clearly different. Moreover, in the unit cell analysis, the solution of the eigenvalue problem lacks of any consideration about damping, while the most critical issue of the employed material has shown to be this. For this reason, the FE model of the finite structure has been refined by means of proportional damping, which best fit experimental results when its parameters are of the order of 10^{-6}.

It is worth to notice that, despite pillars are meshed in a different fashion with respect to the unit cell model, the amount of nodes employed to describe them is of the same order. Nevertheless, the computational time needed to perform the two analysis is comparable, as the solution of eigenvalue problems of the kind of Equation (2.16) is known to be strongly time-consuming.

Once matrices are obtained, employing mechanical properties indicated in [27], it is possible to write the equation of harmonic damped motion

$$(\mathbf{K} - \omega^2\mathbf{M} + i\omega\mathbf{C})\boldsymbol{x}_\mathbf{0} = \boldsymbol{f}. \tag{3.1}$$

Grouping the dynamic matrix so that $(\mathbf{K} - \omega^2\mathbf{M} + i\omega\mathbf{C}) = \mathbf{K}_{dyn}(\omega)$ and pre-multiplying by its inverse, the displacement field is obtained:

$$\boldsymbol{x}_\mathbf{0} = \mathbf{K}_{dyn}^{-1}\boldsymbol{f}. \tag{3.2}$$

This procedure describes the typical solution of a steady state vibration problem. Indeed, the assumptions of harmonic, synchronous response have been made. Equation (3.2) is solved for each value of ω in order to collect the data to build frequency-dependent transfer functions for each point of the specimen. The excitation is applied to all the three nodes in the thickness of a point of the surrounding plain plate. Only out-of-plane excitation has been prescribed.

The boundary conditions applied to model, showed in Figure 3.12, are derived from the experimental setup in which a clamp held the plate from the bottom while the excitation was prescribed at the top.

3.2.2 Results

The first interesting result is the frequency response function of a node of the plate belonging to the pillar forest. This allows to qualitatively characterize some branches in the band structure and to validate the assumptions made about the involvement of the modes. Being a vibration case, some points, especially those in particular positions as the center, could represent nodes in the deformed shape at each frequency, thus being misleading in the evaluation of a band gap. For this reason it is more safe to look at the average of some FRFs and in the present case the average has been evaluated on a big portion of the pillar area. This, albeit does not technically qualifies as a frequency response function, delivers an idea of the transmission in the zone.

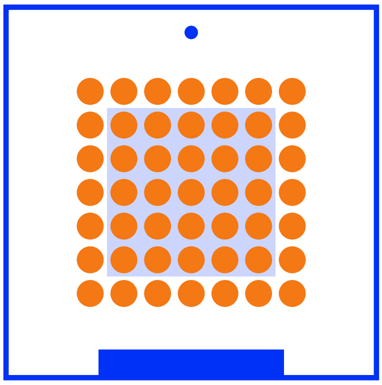

Figure 3.12: Scheme of the constraints and the excited point. The shaded area is the one over which the transmission is evaluated.

In Figure 3.13 the plot of the transmission, which in this case is evaluated as a displacements ratio has been attached to the band structure to allow an easier comparison between them. It has to be said that the limit of one tenth represented by the orange line in the transmission plot is absolutely arbitrary, meaning that there is no formal rule to distinguish transmission bands from band gaps. Thus, the lowering of one order of magnitude is just a reasonable guess.

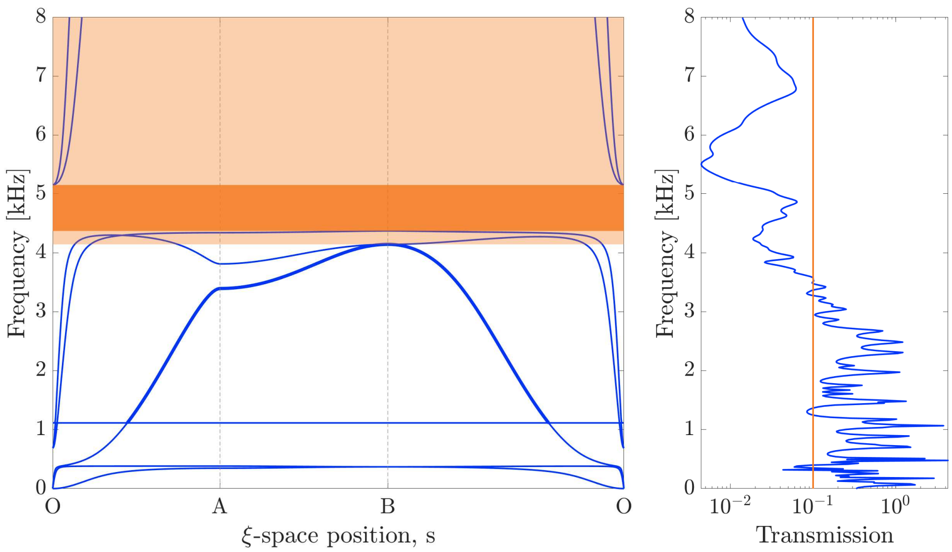

Figure 3.13: Band structure and transmission up to 8kHz. In the latter, the orange line indicates a transmission of one tenth.

The band structure predicts the onset of the band gap to be around 4100Hz while the average of the transmission becomes lower than one tenth at 3600Hz, which can be indicated as a cut-off frequency. The steady state simulation of the finite lattice seems to agree with Bloch analysis, upholding the idea that the stressed branch of the band diagram is the one describing the main mechanism triggered by out-of-plane excitation at this frequency range.

Albeit the difference between these two frequencies can be due to the choice of the threshold in the transmission plot, it can be useful to investigate other possible cause. As first it should be mentioned damping, as the band structure does not contain this information while the transmission can be indeed lowered by an high damping. Moreover, also modes of the whole specimen could affect transmission and even the two peaks in the band gap range could be due to this. Eventually, mechanical properties provided in [27], and especially the elastic modulus, are given in the form of wide ranges because of the manufacturing dispersion and this analysis is carried out considering the average values. Thus, a more refined mechanical characterization could lead to an even better agreement.

Another way to check Bloch analysis predictions is to plot another transmission which is also function of the output point through the whole plate, and thus obtaining a two-dimensional color map describing the middle plane of the plate at each frequency. For this reason, it is necessary to select some particular frequency values to better analyze the phenomenon, and in Figure 3.14 results are shown from 2kHz to 5kHz with 1kHZ steps. As a side note, despite it is possible to elaborate results to obtain the behavior of the middle plane, it would be better to prevent the issue making sure that the mesh present that layer.

Figure 3.14(a) shows the transmission for a frequency at which more than one branch exist in the band structure and, among these, there is the one that has been individuated as a reference for flexural behavior. Indeed, energy can enter the pillar forest and be of the same order of magnitude of the energy outside the forest. This image also clarifies the importance of evaluating the transmission in different points of the pillar area as the presence of either nodes or very compliant points can be misleading when the frequency response function is plotted. Similar considerations can be made for Figure 3.14(b) in which the approach to the band gap seems to prevent the energy to easily penetrate the pillar area although energy is still clearly present in it. Also, despite transmission near the top edge is higher than the one in the forest, on both the left and the right side it is lower to the point to be comparable to the inner one.

When the focus moves to higher frequencies the lack of transmission in the central square becomes unequivocal for most of the area, as it is shown in both Figure 3.14(c) and Figure 3.14(d). The former belongs to a frequency region predicted to allow transmission by Bloch analysis while, from this steady state test, one would expect to see clear signs of band gap. Indeed, since the transmission plot presented in Figure 3.13 and these plots are two different ways to represent the same results, they agree to each other. The reason why the energy is localized only along the edge close to the excitation is not clear and, as it has been said about the average transmission

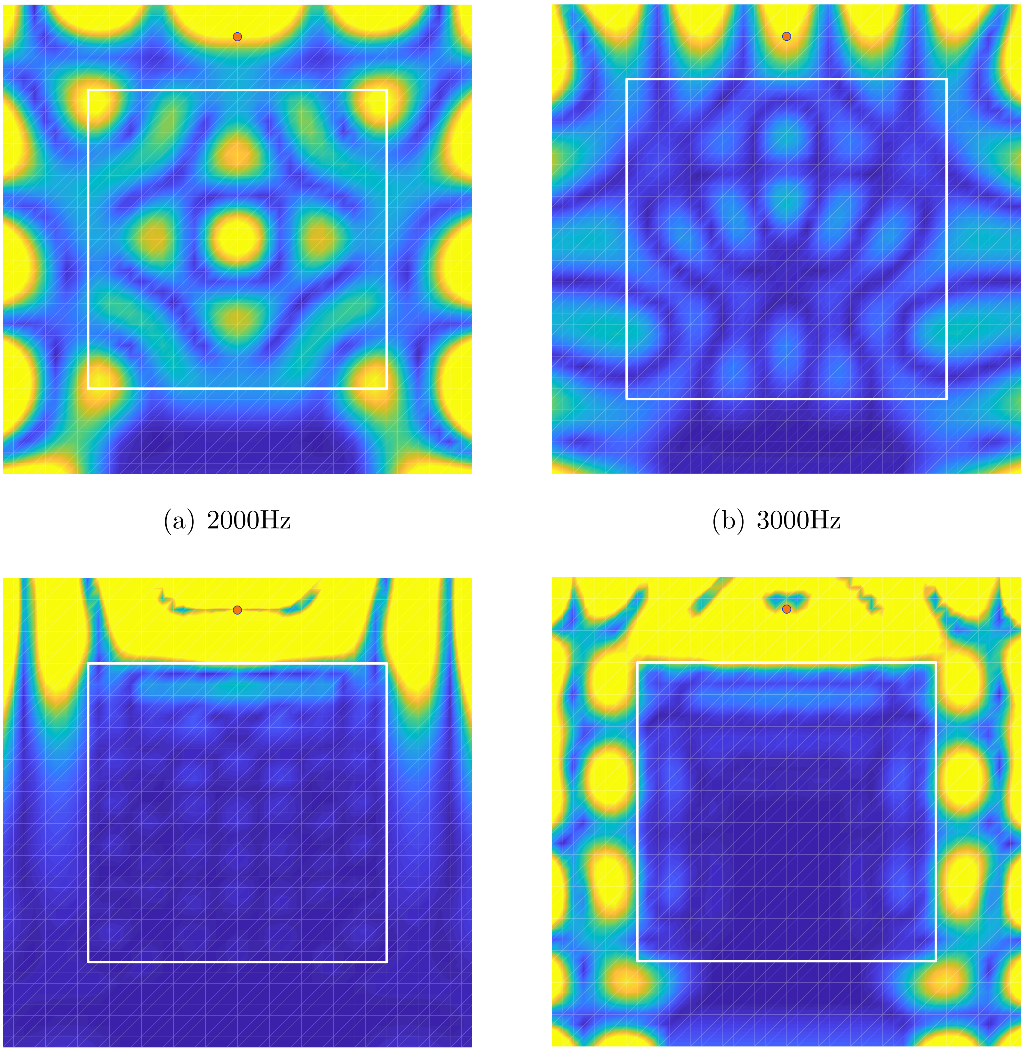

(a) 2000Hz

(b) 3000Hz

(c) 4000Hz

(d) 5000Hz

Figure 3.14: Color representation of the transmission, evaluated as out-of-plane displacements ratio, in the middle plane of the plate at four different frequencies. White squares show the boundaries of the lattice. Orange dots are the excitation points.

in the pillar area, this could be due to particular modes of the structure itself. Eventually, last image depicts a full band gap region: energy is clearly localized outside the central square and even in the further zones of the plate the transmission is quite significant.

The observation of Figure 3.14 allows to unfold two more interesting ideas. The first comes from a comparison of these maps with the scheme in Figure 3.12 that shows how the constraint at the bottom does not reach the pillar forest so that a portion of plain plate exist between these two. Thus, one could wonder why the transmission is always prevented in that area, even at 2kHz for which the whole plate is energized. To answer this it is important to keep in mind the physical origin of this results, namely the steady state interplay between direct and reflected waves. Thus, the above-mentioned region allows waves to flow through it, but with the condition that these fit there. This means that longer, low-frequency, waves can not find enough space to enter that zone and the end of the transient does not change this condition. It can be shown that for frequencies above 8kHz that zone can indeed store energy.

The second idea to explore is also related to one of the main questions behind this work: the mechanisms involved when band gap feature shows up. Looking at Figure 3.14(c) and Figure 3.14(d) it is possible to notice that some energy is transmitted trough the first row of pillars. This is caused by the action of the resonators themselves that involve the plate beneath them when they are activated. This clarifies that in the occurrence of band gap, the energy is trapped by the pillars moving together with the plate beneath them. For this reason there can not be a full agreement between the onset of the band gap predicted by Bloch analysis and the equivalent mode extracted through a modal analysis carried out considering the resonator alone clamped at the bottom. In Figure 3.14(d) this happens not only on the edge of the forest facing the excitation point and the phenomenon looks localized where higher transmission is available, all around the pillar area.

Figure 3.15 shows the three-dimensional rendering of the cases in Figure 3.14. Geometries follows the actual deflected shape while colors highlight the transmission obtained again as a displacements ratio, although here all the three components are taken into account through the modulus. Moreover, damping leads to different phase delays across the structure and the deflected shapes take this into account since not all the points are at the maximum of their motion. Instead, the color map depicting the transmission do not consider this comparing only the amplitude of the oscillations. Somewhere, thus, colors could highlight spot looking very little compliant, but this should not confuse the reader.

Figure 3.15(a) show a distribution of the energy not uniform but however spread among all the plate and the resonators. Some of the latter are greatly compliant and some other less, probably due to the wavelength involved, and the same can be said for the plate beneath. In Figure 3.15(b) the behavior of the plate is almost the same as the former, although the lower overall transmission is evident. Figure 3.15(b) is helpful to the concerns expressed above, namely the understanding on the behavior of the first rows of pillars. Despite Figure 3.14(c) presents a light sign of transmission in the upper part of the forest area, in Figure 3.15(c) resonators located there trap an important amount of energy without the participation of their bases. This is a key feature as the energy can travel from a cell to another only through the plate. The motion of compliant pillar mostly results in a tilting of the head of the pillar.

Eventually, in Figure 3.15(d) the resonators involved are those along the three edges of the forest that do not face the constraint. Their motion is very little compared to the previous case while the plain plate is able to store more energy. Here it can be stated easily that the frequency belongs to a band gap.

Looking at the last two images just described, another consideration can be done. The idea of a strong activation of the resonators in the neighborhood of the onset of the band gap, due to the presence of a resonance of the stand-alone pillar, could be supported by the comments made about Figure 3.15(c). Nevertheless, increasing the frequency of the excitation, the filter characteristic of the lattice remains while the energy trap at the hand of resonators ceases. Hence, the idea of a level of energy that the lattice can not elaborate seems to suit better these results and thus no comparison with dynamic absorbers case can be made, despite the stationariness of the analysis. Moreover, it should be reminded that dynamic absorbers only allow to place anti-resonances at specific frequencies, and they can not prevent motion for such wide bands as in the present case.

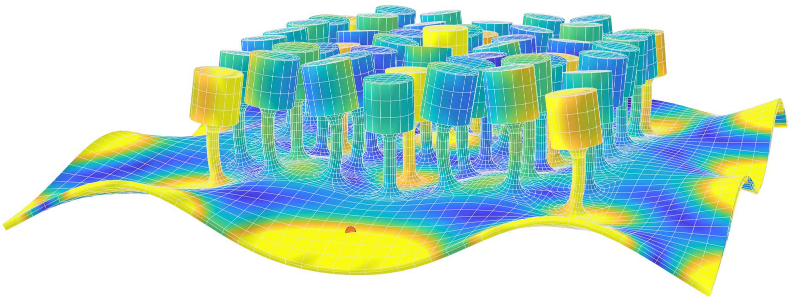

(a) 2000Hz

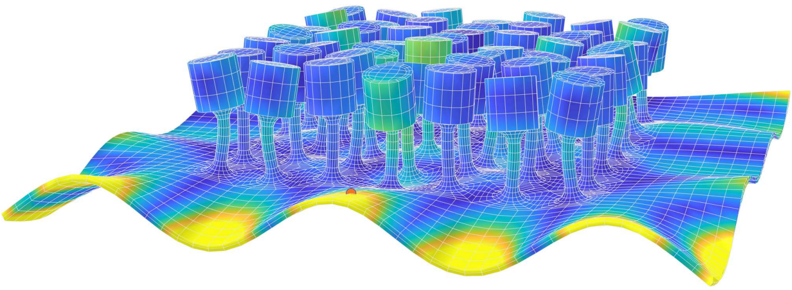

(b) 3000Hz

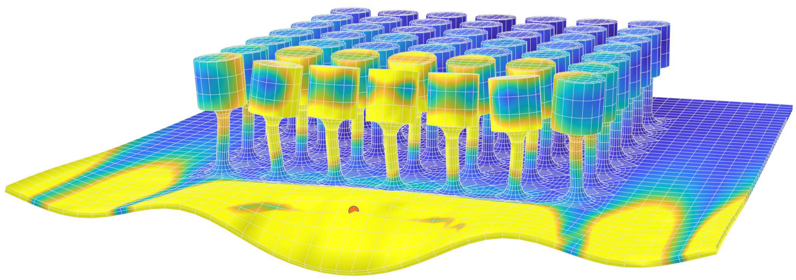

(c) 4000Hz

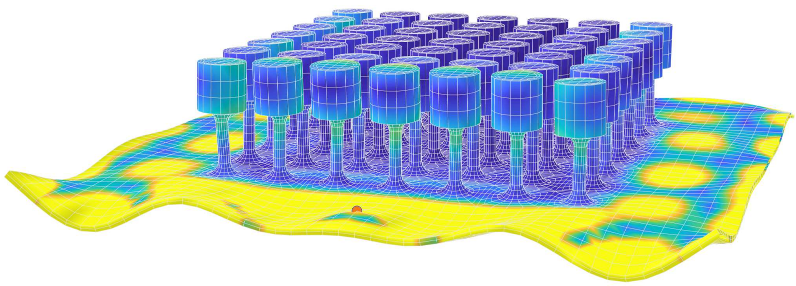

(d) 5000Hz

Figure 3.15: Color representation of the transmission, evaluated as total displacements ratio. Exaggerated deflections are represented taking into account the phase. Orange points locate the excitation.

3.3 Experimental test

The characteristics of numerical simulation illustrated in the previous section, like the nature and position of constraints and force, has been defined starting from the experimental setup employed. Thus, what is expected from experimental results is to support the numerical simulations and show the same mechanisms, keeping in mind the limits of experimental test with respect to simulations. Nevertheless, it should be said that the level of completeness achieved by means of the available tools is great, especially considering the very little effort needed to obtain them thanks to the laser vibrometers.

Furthermore, it is worth to remind that test have not been carried out at the end of the design process with the only purpose of validate numerical simulations, but instead they led to modifications of the geometry playing as crucial a role as the manufacturing aspects.

After a brief presentation of the setup and the tools employed, results will be provided in a comparative fashion with the numerical case, while the nature of the mechanisms involved has been already unfolded in the previous section.

3.3.1 Setup and measurement

All the experiments here presented have been carried out in the *Imaging Lab* of the *Civil, Environmental and Geo- Engineering Department* of the *University of Minnesota*. Figure 3.16 presents some pictures of the laboratory and of the specimen in measurement setup. In the specific, Figure 3.16(a) allows to see how the out-of-plane excitation has been provided by the shaker through the stinger. In Figure 3.16(b) the plain side of the plate is shown and an unfocused laser beam is visible on it; this face has been covered with reflective tape to increase the performances of the lasers, as will be soon explained. Figure 3.16(c) delivers an overall view of the measurement station, with the lasers on their tripods on foreground and the PC on the right. The latter is an assembly of the five blue units in the rack: starting from the bottom the three boards that control a laser head each, the junction box that collects signals from all the laser controllers and, on the top, the actual PC. Eventually, in Figure 3.16(d) a front view of the lasers is given and before the central one the camera can be seen. This allows to visualize the specimen on the screen and to guide the lasers through it.

In Figure 3.16(c) the screen shows the Polytec software for the acquisition. Two preliminary alignments are required: a 2D alignment that makes the system understand the dimensions of the specimen, and a more time-consuming 3D alignment by means of which the position and the orientation of the measured surface is detected. Once the alignment is done, measurement point are selected. Eventually, since the same software generates the signal and send it to the amplifier placed before the shaker, also this selection is made.

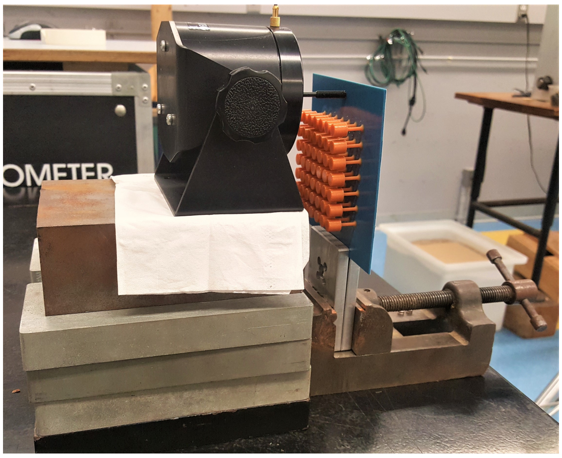

(a)

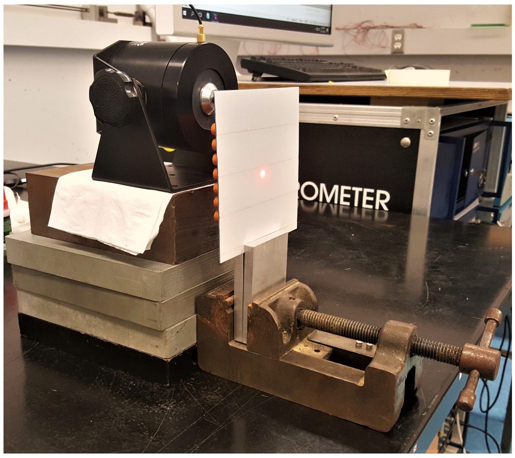

(b)

(c)

(d)

Figure 3.16: Experimental setup.

The operating principle behind the measurements of these sensors, as explained in [26], involves an interferometric measure called laser Doppler vibrometry: when the beam reaches the measured surface is scattered back with a slight shift in frequency, which is proportional to the velocity of the scanned point. When the scattered laser is caught by the sensor, and to improve this the reflective tape is applied, its signal is superimposed to a reference one obtained by splitting the original beam. The resulting intensity is what is detected and manipulated to obtain velocities. Eventually, a Bragg cell adds a phase shift that allows to understand the direction of the motion.

3.3.2 Results and comparison

When a steady state analysis is required over a range of frequencies, two kind of signal provide better performances: a white noise and a periodic chirp. While the former contains every frequency in the range at any time instant, the latter increases its frequency with time to span the entire band. After some attempts, the periodic chirp has shown to be more suitable for the test, especially since measures has been repeated tenfold to get an average and thus lowering the noise in the signal. This leads to a remarkable growing in the time required to complete the analysis and periodic chirp is able to trigger the acquisition more quickly.

Likewise for the numerical analysis, the first result to check is the transmission from the excitation point to the pillar area of the plate. Again, similarly to that case, the area taken into account to evaluate the function is the one under all the pillars but the outermosts. In Figure 3.17 the experimental transmission is plotted with the band structure, in the same fashion of Figure 3.13. Here the drop of transmission occurs at frequencies slightly lower than 4kHz and it is even more clear than in the numerical case.

Figure 3.18 shows the comparison between the numerical and the experimental transmissions. The first attention should be paid to the frequency at which the transmission drop occurs. This has been predicted to be in the neighborhood of 4kHz by both the Bloch analysis and the numerical simulations. The experimental result confirm this prediction as it cross the chosen threshold of one tenth around 3600Hz.

This comparison has been also the reference in the tuning of the proportional damping parameters employed in the numerical simulations. The chosen parameters, at the end, have been both equal to $1 * 10^{-6}$ although also values of $2 * 10^{-6}$ or $3 * 10^{-6}$ fit the experimental curve. The reason why these values have been discarded, albeit they were even more consistent than the chosen one before and after the cut-off, with lower peaks, is that it could not be found a greater agreement between the transmission drops. In those cases, even if the transmission at low frequencies was always overestimated, the transition to the stop band was less steep, with lower initial frequency.

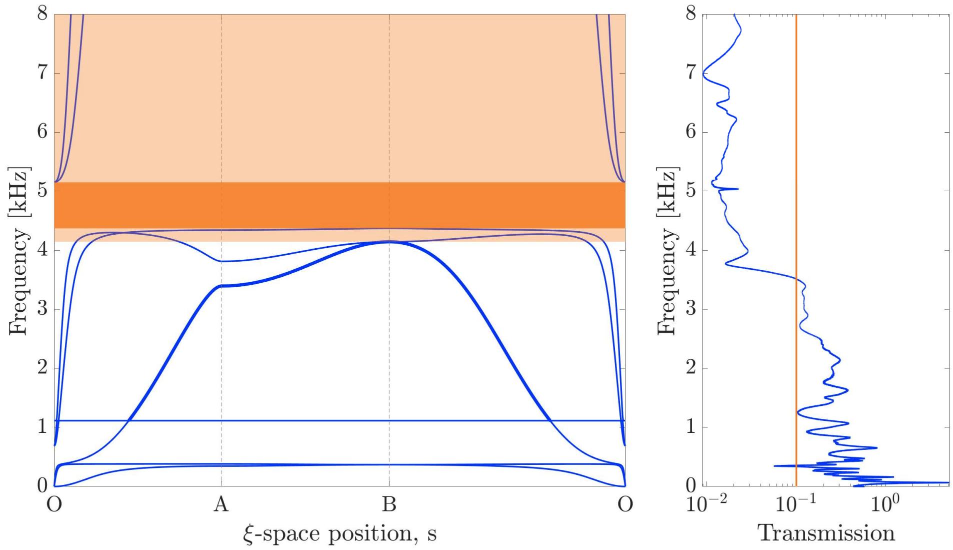

Figure 3.17: Band structure and experimental transmission up to 8kHz. In the latter, the orange line indicates a transmission of one tenth.

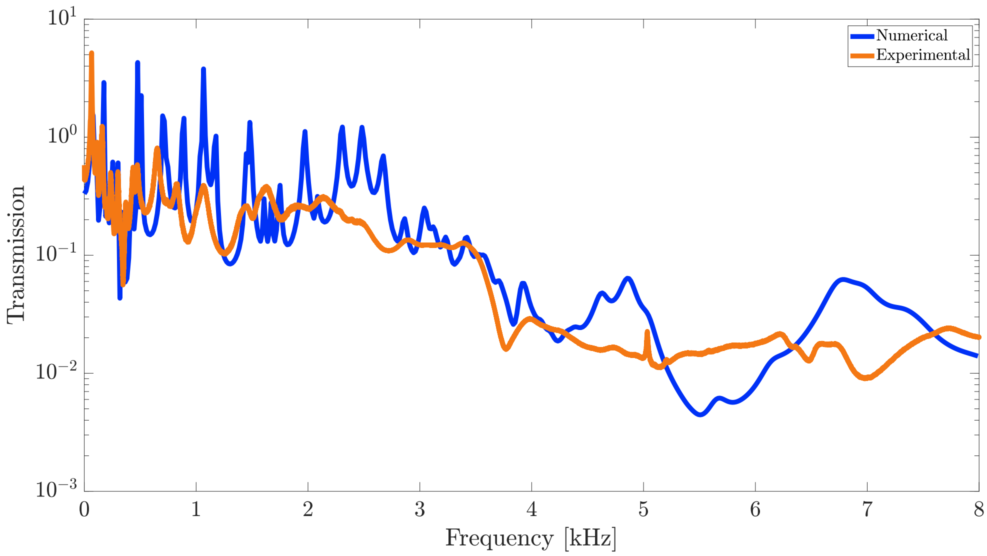

Figure 3.18: Comparison between numerical and experimental tranmission.

In Figure 3.19 the same transmission maps showed in Figure 3.14 are proposed for the experimental results. The lower frequencies depicted in Figure 3.19(a) and Figure 3.19(b) present a decent energy spread. Despite most of the activation is in the neighborhood of the excitation point, the amount of energy that enter the resonator area is definitely comparable with that stored in the surrounding plain plate. As the frequency raises, transmission drops and very little energy enter the pillar forest. This is the case of Figure 3.19(c) and Figure 3.19(d): despite the area beneath the resonators has shown to be little energized even at lower frequencies, here the energy reach most of the sitting plate, especially in the last case, and it can be seen a significant difference between the the inner and the outer portion of the plate.

When these plots are compared with the numerical equivalents, as done in

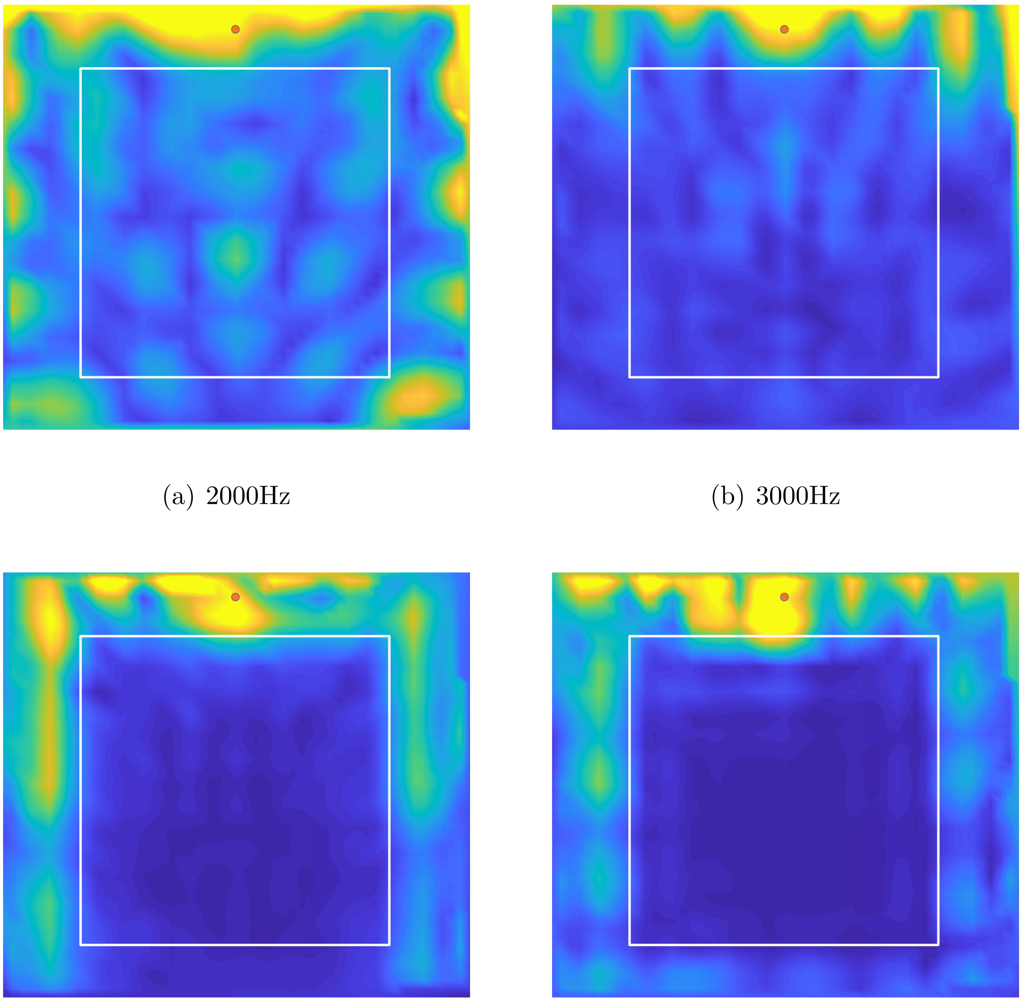

(a) 2000Hz

(b) 3000Hz

(c) 4000Hz

(d) 5000Hz

Figure 3.19: Color representation of the transmission, evaluated as out-of-plane velocities ratio, in the middle plane of the plate at four different frequencies. White squares show the boundaries of the lattice. Orange dots are the excitation points.

Figure 3.20, a good agreement is found. It is evident that the energy able to be transmitted is less in the experimental case, suggesting an underestimated damping, although several similarities can be highlighted. Before doing this, however, it is convenient to underline the different dimensions of the two set of plots: the experimental maps are smaller because the measured points in the experiment could not be placed at the very edges of the structure since the different laser beams could fail to catch it. So the interpolation of these results involve a smaller portion of the whole plate. For example, while the numerical maps show the uncompliant region interested by the clamp, the experimental plots lack of that zone.

Focusing on the two frequencies in the stop band, it is interesting to notice how the behavior of the external plate is well predicted by the numerical simulations. In Figure 3.20(c) the energy surrounding the forest displaces with two big chunks at the two sides and the experimental result even displays a better transmission. In Figure 3.20(d), instead, transmission is localized in few spots correctly predicted by the numerical model. The damping here is clearly higher in the experimental case although, at the bottom of the plate energy is able to enter the space between the clamp and the pillars, while the numerical simulation lacks of this prediction.

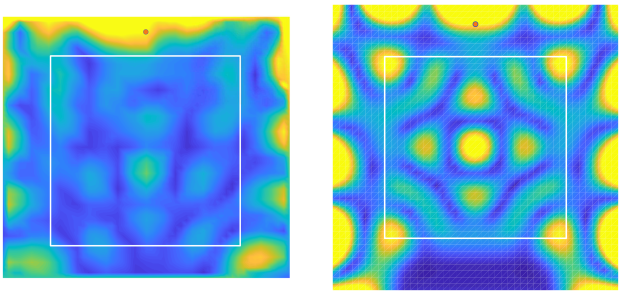

(a) 2000Hz

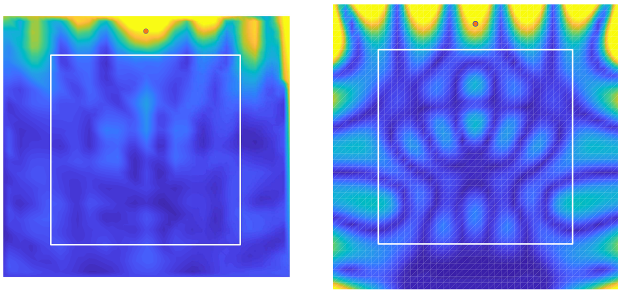

(b) 3000Hz

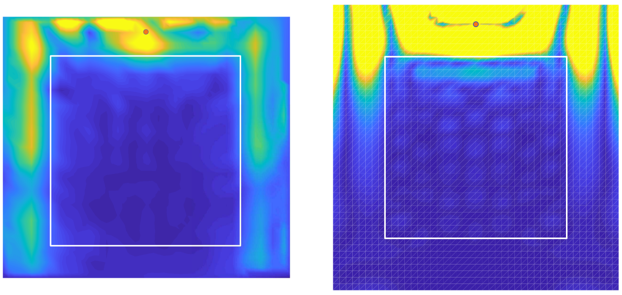

(c) 4000Hz

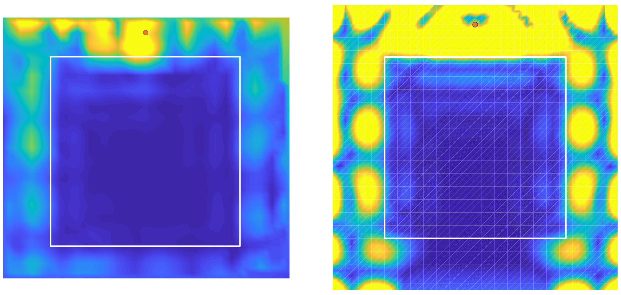

(d) 5000Hz

Figure 3.20: Comparison between numerical (right column) and experimental (left column) transmission.

3.4 Numerical transient simulation

Being the specimen obtained through additive manufacturing, its properties have been the sum of manifold aspects. For the concerns of this work, the most conditioning characteristics have been the dimensions and the damping. When the propagation of an acoustic wave has to be observed, there should be enough time for the wave to fully develop before any reflection from the boundaries occurs. What is usually done to achieve this ability is to use greater specimen. Unfortunately, so far it is still not possible to manufacture big parts with this kind of printer, and even the maximum dimension allowed, about 50cm, would not be sufficient to allow the measure. Furthermore, even supposing to be able to manufacture such a big structure, the high damping emerged from the experimental test, see Figure 3.20, would not allow the wave to travel for so long.

Despite this, it is of course possible to carry out numerical simulations with lower, or absent thereof, damping and this is what this section is about. Particularly, it will be presented the simulation of an out-of-plane wave showing directionality, relying on the results of Figure 2.10, page 27. There, Figure 2.10(f) showed a pronounced directionality when the frequency approach the maximum of that mode.

In order to satisfy to the best the requirements told above for the analysis of the transient, a square lattice of 32x32 cells has been considered. After a remarkably time-consuming assembly of the mass and stiffness matrices, an interative time integration has been operated by means of the Newmark implicit method. A burst of the kind of Figure 2.9, page 24, has been generated as input signal with a central frequency of 3600Hz, notwithstanding this has shown to be the cut-off frequency for the finite dimensions lattice. Indeed, the present simulation has been carried out for the undamped case only for the reasons just explained. Moreover, directionality is a feature that is often observed at the highermost frequencies of modes, where surfaces fold due to the periodicity and dispersion relations cease to be cone-shaped. The excitation is provided at the center of the plate and displacement, velocity and acceleration fields are obtained at each time instant.

In order to visualize the main paths for phase propagation, the best way is to plot displacements, since following a peak means following a constant phase value in the wave. This is done in the left column of Figure 3.21, on which the spatial distribution of phase velocity showed in Figure 2.10(d) is depicted.

When the attention moves to group velocity, highlighting preferential patterns it is not as straightforward as for the phase velocity. In the backgrounds chapter it has been said that group velocity is that at which energy travels, as both these quantities are related to the envelope of the wave packet. Since there is not a direct way to plot the envelope of the wave packet, what is done is to rely on field properties that are able to catch the particular mechanisms. Thus, when the object of the study is in-plane behavior it is usually considered the divergence of the field being it able to capture the small displacements involved in this case. On the other hand, when flexural mechanisms are analyzed, the best option is to look at the curl of the field, since it is more affected by deflected shapes of this kind. This is what is shown in the right column of Figure 3.21, where also the group velocity plot of Figure 2.10(f) is depicted.

The first selected time instant of Figure 3.21(a) has been picked at an intermediate stage of the excitation. At this point the wave packet is not completely formed yet. The outermost peak of the displacement field is still pretty close to the excitation point although it should be said that the fast, small in-plane components, which can be seen lowering the threshold of the colormap, already reached the edges. This gives an idea of the dimensions of the specimen required to get rid of any scattering during the measurement. On the right, group velocity patterns are already visible despite the early stage, and they clearly distribute along the predicted directions, namely the bisectors of each quadrant.

In Figure 3.21(b) the time instant in which the excitation ceases is represented. From this moment on, the plate is free to move and the energy of the system is constant. The displacement field maintains a mostly circular profile: even though the yellow area depicting a peak presents some light corners along the vertical and the horizontal directions, the inner blue area seems to promote the diagonal patterns. The conclusion is that none of this light traces is enough to address for directional behavior. On the contrary, the curl still shows different characteristics between diagonal and main directions. Remembering that this is just a qualitative descriptor, some channel-like activation is visible at the corner of the plate, albeit, closer to the excitation, main direction looks to be more energized.

The time interval between the second and the third time instants considered, with the latter showed in Figure 3.21(c), is half the duration of the burst. Here the reflection of boundaries can not be neglected anymore as the wave front completely invested them. The phase is still propagating without directionality as crests still distribute in a circular fashion. The energy, instead, increases its concentration along diagonal directions, again with channel-like activation. The cross-shaped pattern is now definitely clear, supporting the prediction made looking at group velocity plots.

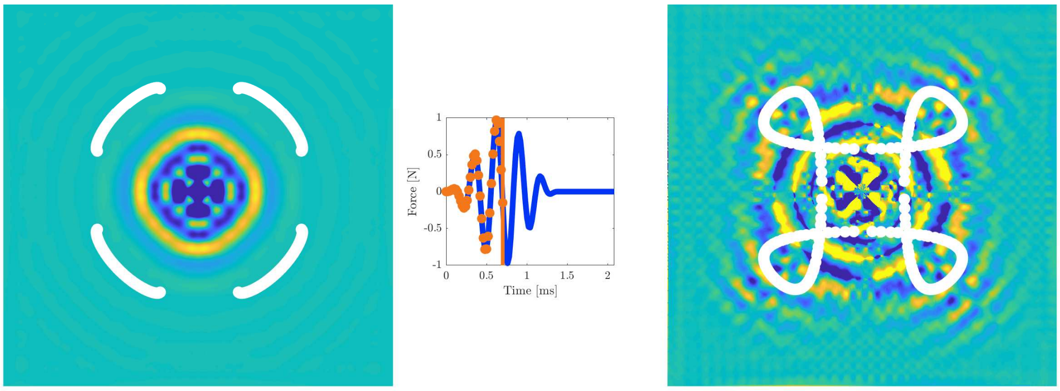

(a)

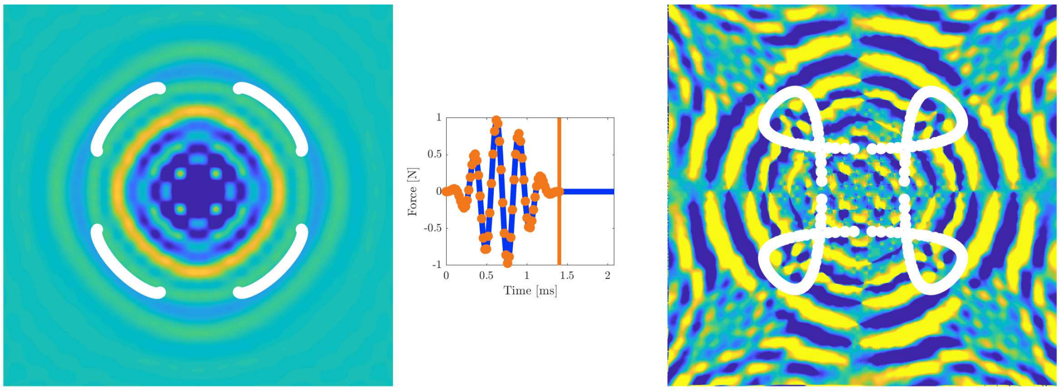

(b)

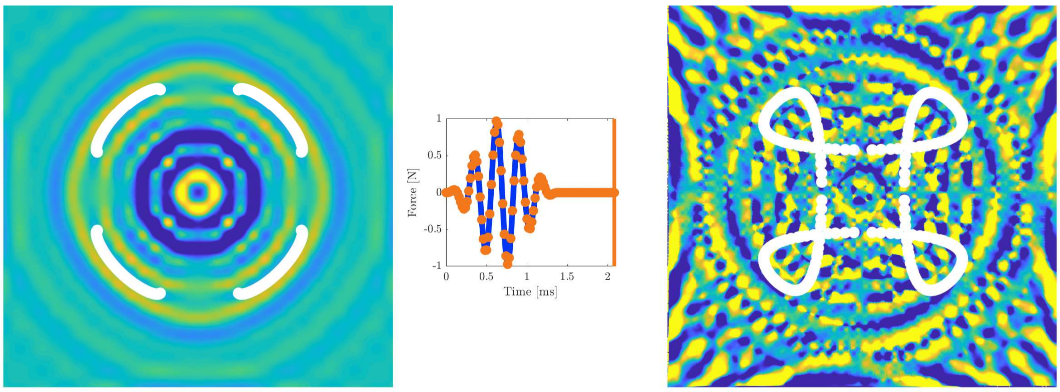

(c)

Figure 3.21: Out-of-plane displacement with superimposed phase velocity (left column) and curl of the displacement field with superimposed group velocity (right column). The central column shows the excitation up to the considered time instant with orange dots representing time steps.

Chapter 4

Conclusions

The present work has been thought to analyze some classical phononic features of periodic structures by means of innovative tools and techniques, able to unfold some of the less understood mechanisms involved. In particular, the case of locally resonant phononic crystal has been taken into account and both numerical simulations and experimental test have been carried out. The main feature sought has been the filtering capabilities of these structures in their band gap.

Without any doubt, the most important tool for the modeling of the lattice is Bloch analysis, which allows to study the behavior of an infinite lattice analyzing an elementary unit only. This is realized through the application of some clever boundary conditions that enrich the model with the information about the infinite repetition. The structure to which these conditions are applied is modeled by means of a full three-dimensional finite element model employing hexaedra elements. This represents one of the innovations mentioned since such plates are commonly described using plate elements, although in that way it could not be possible to describe complex resonators that extend out of the plate plane. After the application of periodic boundary conditions, dispersion relations are derived solving an eigenvalue problem for any value of the wave vector. The novelty brought by the full three-dimensional model has been the appearance of several modes related no more to the plate but only to the resonators. Indeed, the solution of an eigenvalue problem returns a modal characterization involving the whole structure and can not neglect modes whose mode shapes are localized in the resonator. Thus, a more careful sight is required for the interpretation of results, as those that could appear as full band gaps in two-dimensional models can become modal band gaps within the full model.

Once the lattice has been characterized, the design process of a finite lattice has started in order to find a suitable geometry. This design encompassed several aspects which represented some of the other new techniques employed. Indeed, it has been chosen to test additive manufactured specimen and thus the first important constraint has been given from this. Additive manufacturing allow the realization of very complex geometries that would have been terrifically expensive, when possible, if produced with classical techniques. Nevertheless, the technology available in the field can not get rid of the significant limitations about dimensions, which are usually confined to some centimeters. Moreover, for delicate structures like the one presented in this work, the use of mechanically removable supports have shown to be unemployable since there has been no chance to clean the specimen without irremediably breaking it.

Unfortunately, additive manufacturing also indirectly led to even more restrictive constraints given, this time, by the employed material: after first test it already shown an high internal damping that has not allowed to use specimens of appropriate dimensions and thus to analyze the propagation transient. For this reason, only steady state test have been carried out experimentally, although these found very good agreement with numerical results.

Furthermore, the numerical steady state simulation has given the opportunity to visualize three-dimensional renderings of the structure which have represented a definitive step forward with respect to the classical two-dimensional representation of the activation of the plate. The possibility to look at the whole structure permitted to observe the action of the resonators and their activation, highlighting how, in full band gap regions, they loose their capability of storing energy. Also, in the same way it has been possible to evaluate the penetration of the energy in the lattice that has shown to be very little for full band gaps frequencies.

Despite the complete path followed by this work, starting from the unit cell analysis to the experimental validation, some aspects have been kept out of the work despite they would deserve a deeper investigation. At first, it should be mentioned that even though steady state results found a good agreement with Bloch analysis, the latter only describes propagation and the connection between the two has not been clarified yet. What is understood so far, on the author's knowledge, is that even the steady state problem can be seen as a wave propagation one, and the inversion of the dynamic stiffness matrix is only a more convenient tool to get to the result. Moreover, being able to numerically obtain the behavior of resonators, it would be worth to try to get it experimentally, although, even employing laser vibrometers, the measure can be hard due to the great amount of hidden spots due to the close repetition of cells.

Eventually, on the author's opinion, this technology can be a powerful tool in the control of vibrations in any kind of structures, and thus it begs for some applications. So far, damping materials are the solutions in such cases, also because they transform the energy of the vibration into heat without redirecting it into the structure, and this is usually something pursued.

Bibliography

[1] M Badreddine Assouar et al. “Broadband plate-type acoustic metamaterial for low-frequency sound attenuation”. In: *Applied Physics Letters* 101.17 (2012), p. 173505.

[2] L. Brillouin. *Wave Propagation in Periodic Structures: Electric Filters and Crystal Lattices*. International series in pure and applied physics. McGraw-Hill Book Company, Incorporated, 1946.

[3] Paolo Celli and Stefano Gonella. “Heterogeneity meets disorder: anomalous wave transport in telescopic metamaterials”. In: *arXiv preprint arXiv:1703.08522* (2017).

[4] Paolo Celli and Stefano Gonella. “Manipulating waves with LEGO® bricks: A versatile experimental platform for metamaterial architectures”. In: *Applied Physics Letters* 107.8 (2015), p. 081901.

[5] Andrea Colombi et al. “Directional cloaking of flexural waves in a plate with a locally resonant metamaterial”. In: *The Journal of the Acoustical Society of America* 137.4 (2015), pp. 1783–1789.

[6] Andrea Colombi et al. “Forests as a natural seismic metamaterial: Rayleigh wave bandgaps induced by local resonances”. In: *Scientific reports* 6 (2016), p. 19238.

[7] Enrico Fermi et al. *Studies of the nonlinear problems*. Tech. rep. Los Alamos Scientific Lab., N. Mex., 1955.

[8] Christophe Geuzaine and Jean-François Remacle. “Gmsh: a three-dimensional finite element mesh generator with built-in pre-and post-processing facilities (2008)”. In: *URL: http://www.geuz.org/gmsh* (2008).

[9] Stefano Gonella and Massimo Ruzzene. “Analysis of in-plane wave propagation in hexagonal and re-entrant lattices”. In: *Journal of Sound and Vibration* 312.1-2 (2008), pp. 125–139.

[10] Weijian Jiao and Stefano Gonella. “Intermodal and Subwavelength Energy Trapping in Nonlinear Metamaterial Waveguides”. In: *Physical Review Applied* 10.2 (2018), p. 024006.

[11] Weijian Jiao and Stefano Gonella. “Mechanics of inter-modal tunneling in nonlinear waveguides”. In: *Journal of the Mechanics and Physics of Solids* 111 (2018), pp. 1–17.

[12] W. T. Baron Kelvin. *Popular Lectures and Addresses: Constitution of Matter*. Vol. 1. Macmillan and Company, 1889.

[13] Jensen Li and Che Ting Chan. “Double-negative acoustic metamaterial”. In: *Physical Review E* 70.5 (2004), p. 055602.

[14] Ting-Wei Liu and Fabio Semperlotti. “Experimental evidence of robust acoustic valley Hall edge states in a topological elastic waveguide”. In: *arXiv preprint arXiv:1803.04910* (2018).

[15] Zhengyou Liu et al. “Locally resonant sonic materials”. In: *science* 289.5485 (2000), pp. 1734–1736.

[16] M Miniaci et al. “Observation of topologically protected helical edge modes in Kagome elastic plates”. In: *arXiv preprint arXiv:1710.11556* (2017).

[17] S Hossein Mousavi, Alexander B Khanikaev, and Zheng Wang. “Topologically protected elastic waves in phononic metamaterials”. In: *Nature communications* 6 (2015), p. 8682.

[18] VF Nesterenko. “Propagation of nonlinear compression pulses in granular media”. In: *Journal of Applied Mechanics and Technical Physics* 24.5 (1983), pp. 733–743.

[19] Mourad Oudich et al. “Experimental evidence of locally resonant sonic band gap in two-dimensional phononic stubbed plates”. In: *Physical Review B* 84.16 (2011), p. 165136.

[20] Yan Pennec et al. “Low-frequency gaps in a phononic crystal constituted of cylindrical dots deposited on a thin homogeneous plate”. In: *Physical Review B* 78.10 (2008), p. 104105.

[21] A Srikantha Phani, J Woodhouse, and NA Fleck. “Wave propagation in two-dimensional periodic lattices”. In: *The Journal of the Acoustical Society of America* 119.4 (2006), pp. 1995–2005.

[22] Reza Pourabolghasem et al. “Physics of band-gap formation and its evolution in the pillar-based phononic crystal structures”. In: *Journal of Applied Physics* 116.1 (2014), p. 013514.

[23] John William Strutt Baron Rayleigh. *The theory of sound*. Vol. 2. Macmillan, 1896.

[24] Vìctor José Sánchez-Morcillo et al. “Second-harmonic generation for dispersive elastic waves in a discrete granular chain”. In: *Physical Review E* 88.4 (2013), p. 043203.

[25] Roman Süsstrunk and Sebastian D Huber. “Observation of phononic helical edge states in a mechanical topological insulator”. In: *Science* 349.6243 (2015), pp. 47–50.

[26] *User Manual - Laser Doppler Vibrometer*. Man-Vib-OFV3001-1202-05e. Polytec.

[27] *Vero 3D Printing Material Data Sheet*. MDS-PJ-Vero0718a. Stratasys. 2018.

[28] VG Veselago. “Electrodynamics of substances with simultaneously negative electrical and magnetic permeabilities”. In: *Physics-Uspekhi* 10.4 (1968), pp. 504–509.

[29] R Zhu et al. “Negative refraction of elastic waves at the deep-subwavelength scale in a single-phase metamaterial”. In: *Nature communications* 5 (2014), p. 5510.

[30] Sahar Zouari et al. “Formation of band gaps in thin plate with a periodic array of resonators”. In: *S20 Mécanique et conception de matériaux architecturés et de métamatériaux* (2015).